MP-HSIR: A Multi-Prompt Framework for Universal Hyperspectral Image Restoration

Zhehui Wu[1]   Yong Chen[2]   Naoto Yokoya[3,4]   Wei He[1,4*]

[1] Wuhan University   [2] Jiangxi Normal University   [3] The University of Tokyo

[4] RIKEN Center for Advanced Intelligence Project

{wuzhehui, weihe1990}@whu.edu.cn, chen_yong@jxnu.edu.cn, yokoya@k.u-tokyo.ac.jp

Abstract

*Hyperspectral images (HSIs) often suffer from diverse and unknown degradations during imaging, leading to severe spectral and spatial distortions. Existing HSI restoration methods typically rely on specific degradation assumptions, limiting their effectiveness in complex scenarios. In this paper, we propose **MP-HSIR**, a novel multi-prompt framework that effectively integrates spectral, textual, and visual prompts to achieve universal HSI restoration across diverse degradation types and intensities. Specifically, we develop a prompt-guided spatial-spectral transformer, which incorporates spatial self-attention and a prompt-guided dual-branch spectral self-attention. Since degradations affect spectral features differently, we introduce spectral prompts in the local spectral branch to provide universal low-rank spectral patterns as prior knowledge for enhancing spectral reconstruction. Furthermore, the text-visual synergistic prompt fuses high-level semantic representations with fine-grained visual features to encode degradation information, thereby guiding the restoration process. Extensive experiments on 9 HSI restoration tasks, including all-in-one scenarios, generalization tests, and real-world cases, demonstrate that MP-HSIR not only consistently outperforms existing all-in-one methods but also surpasses state-of-the-art task-specific approaches across multiple tasks. The code and models are available at* https://github.com/ZhehuiWu/MP-HSIR.

1. Introduction

Hyperspectral images (HSIs) provide significantly higher spectral resolution than RGB images, as illustrated in Figure 10 (a), making them essential for urban planning [22, 62], agricultural production [42, 56], and environmental monitoring [2, 59]. However, due to various environmental factors and imaging limitations, HSIs are often affected by degradations during acquisition, compromising image quality and
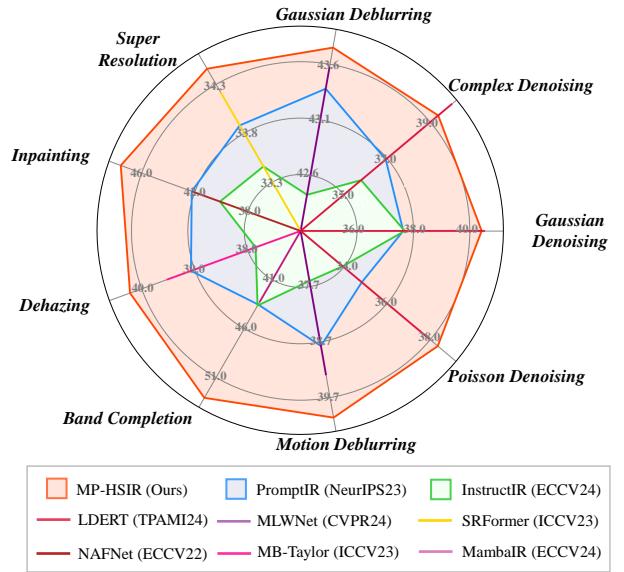
---

*Corresponding author

Figure 1. PSNR comparison with the state-of-the-art all-in-one and task-specific methods across 9 tasks. Average results across all test datasets. Best viewed in color.

limiting subsequent analysis. Consequently, HSI restoration is a critical step in the image processing pipeline.

Despite advancements in task-specific HSI restoration methods [9, 21, 35, 63, 69, 78], the diversity and complexity of degradations pose a significant challenge for a single model to handle multiple HSI restoration tasks. As illustrated in Figure 10 (b), different degradation types have distinct effects on the spectral features of HSIs. For instance, noise increases spectral fluctuations, compression reduces spectral reflectance in certain bands, and haze shifts the spectral curve globally. These diverse impacts hinder the generalization capability of task-specific methods across different scenarios. Therefore, a universal framework is required to address the unique distortions caused by different degradations.

In recent years, all-in-one image restoration methods have achieved significant progress in RGB images [26, 32, 65]. Among these, prompt learning-based approaches [1, 12, 19,
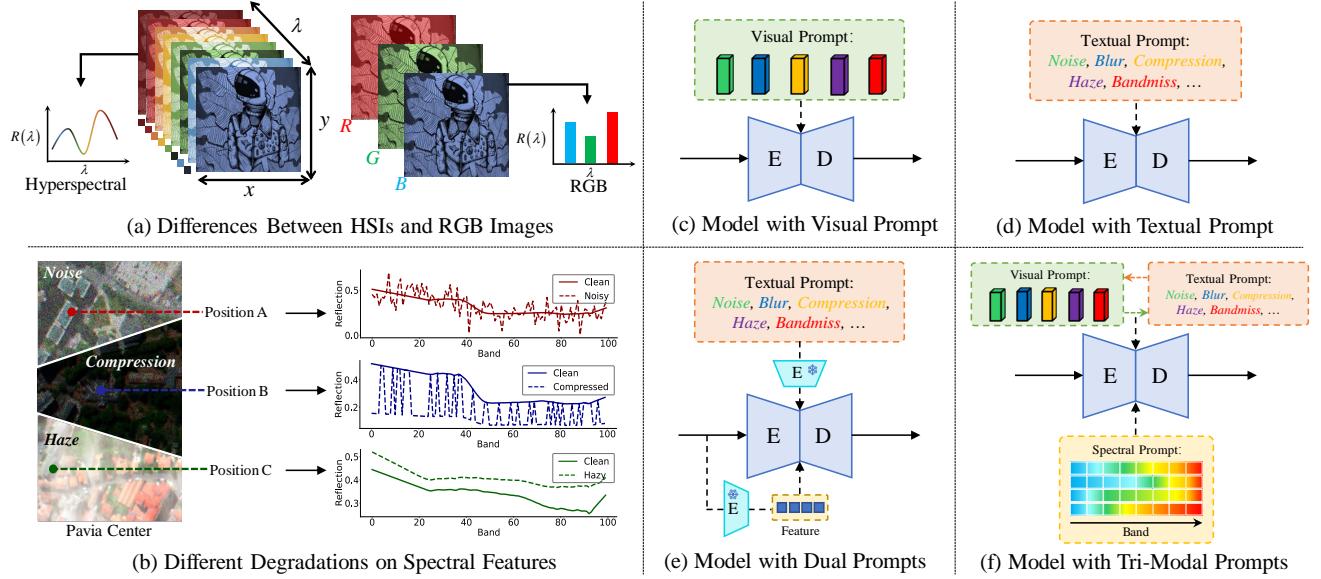
Figure 2. Overview of HSI characteristics and prompt-based all-in-one restoration methods. (a) Differences between HSIs and RGB images. (b) Impacts of different degradations on spectral features. (c) Visual prompt-based models. (d) Textual prompt-based models. (e) Dual-modality prompt-based models. (f) The proposed model integrating spectral, textual, and visual prompts.

36, 44, 52] have garnered attention for their flexibility in task adaptation and efficient degradation perception. Based on prompt modality, these methods can be categorized into visual, textual, and dual prompts. As shown in Figure 10 (c), visual prompt-based models [36, 52] guide restoration by introducing additional prompt components but suffer from limited interpretability. Figure 10 (d) illustrates textual prompt-based models [12, 19], which convert textual prompts into latent embeddings to assist restoration. Nevertheless, inconsistencies may arise when the semantic gap between text and images is too large. Figure 10 (e) depicts dual prompt-based models [1, 44], which leverage pre-trained vision-language models (VLMs) to extract deep representations from text instructions and degraded images, providing more precise degradation guidance. However, existing VLMs still exhibit limitations in modeling HSI degradation information. Specifically, **most all-in-one models fail to consider the unique spectral characteristics of HSIs, often resulting in spectral distortions in the restoration process**.

To address the challenges of all-in-one HSI restoration, we propose a universal multi-prompt framework, MP-HSIR, which integrates spectral, textual, and visual prompts, as illustrated in Figure 10 (f). In this framework, spectral prompts guide the spatial-spectral transformer for spectral recovery, while textual and visual prompts synergistically generate degradation-specific information to guide the global restoration. Specifically, the prompt-guided spatial-spectral transformer comprises two core components: spatial self-attention and dual-branch spectral self-attention. The spatial self-attention captures non-local spatial similarities, while the

the global spectral branch models long-range dependencies in the spectral domain. Meanwhile, the local spectral branch incorporates universal low-rank spectral patterns from the spectral prompts to enhance spectral feature reconstruction. Additionally, the text-visual synergistic prompt deeply fuses the semantic representations of textual prompts with the fine-grained features of visual prompts, enabling controlled restoration while embedding degradation information at the pixel level. As shown in Figure 8, our method outperforms existing all-in-one methods across 9 HSI restoration tasks and surpasses state-of-the-art task-specific methods in multiple tasks. Overall, our main contributions are as follows:

- We propose a novel multi-prompt framework for all-in-one HSI restoration, integrating spectral, textual, and visual prompts. The spectral prompt provides universal low-rank spectral patterns to enhance spectral reconstruction.
- We introduce a text-visual synergistic prompt that combines semantic representations from textual prompts with fine-grained features from visual prompts, enhancing the controllability, interpretability, and degradation adaptability of the HSI restoration process.
- Extensive experiments on 9 HSI restoration tasks and real-world scenarios demonstrate that MP-HSIR significantly outperforms compared all-in-one methods and surpasses state-of-the-art task-specific approaches in multiple tasks.

2. Related Work

2.1. Hyperspectral Image Restoration

Traditional HSI restoration methods mainly leverage prior knowledge, such as non-local similarity [46], low-rank struc-

ture [21, 39], and sparsity [68, 70], to constrain the solution space and employ optimization algorithms [10, 57] to solve the inverse problem. Deep learning-based HSI restoration methods directly learn the mapping between degraded and original images through deep neural networks, including convolutional neural networks (CNNs) [63, 75], transformers [33, 34, 74], and generative models [35]. Although these methods have demonstrated strong restoration capabilities, they are typically designed for specific types of degradation, such as noise removal [6, 29, 67], super-resolution [64, 78], and dehazing [45, 69], lacking universality and adaptability in practical applications.

Recent studies [28, 48, 50, 74] have explored using a single model for multiple HSI restoration tasks. DDS2M [48] designs a self-supervised diffusion model, while HIR-Diff [50] projects HSI into RGB space to leverage a pretrained diffusion model for restoration. Nevertheless, these approaches frequently demand intricate hyperparameter tuning and exhibit slow inference speeds. Furthermore, they fail to adequately account for the distinct characteristics of different degradation types, limiting their effectiveness.

2.2. All-in-One Image Restoration

All-in-one image restoration [26, 44, 65] aims to establish a unified deep learning framework for restoring images with various degradations. However, developing an effective degradation-aware mechanism to distinguish different degradation remains challenging. AirNet [32] addresses this by employing contrastive learning to extract degradation representations, while HAIR [7] leverages a degradation-awareness classifier to capture global information and adaptively generate parameters via a hyper-selection network.

Recently, prompt learning [31, 43] has emerged as a promising paradigm for all-in-one image restoration due to its inherent flexibility and task-specific adaptability. PromptIR [52] integrates visual prompts for dynamic guidance, while PIP [36] refines them into degradation-aware and basic restoration prompts. To enable more controllable restoration, InstructIR [12] utilizes manually crafted instructions to guide the restoration process. Moreover, with the rise of VLMs, several studies [1, 44, 53] have explored the use of pre-trained VLMs to encode both textual and visual information for identifying degradation types. In the field of all-in-one HSI restoration, PromptHSI [30] introduces a text-to-feature modulation mechanism that applies textual prompts to composite degradation restoration in HSI, but it remains inherently limited to a single degradation mode. Overall, existing prompt-based all-in-one methods struggle to effectively characterize different degradation types in HSIs and lack guidance for spectral feature restoration.

3. Method

In this section, we present the multi-prompt framework for universal HSI restoration. First, we review the task of HSI restoration in 3.1. Then, we describe the overall architecture of the MP-HSIR framework in 3.2. Finally, we introduce the Spectral Self-Attention with Prompt Guidance module and the Text-Visual Synergistic Prompts module in 3.3 and 3.4.

3.1. Preliminary: Hyperspectral Image Restoration

HSI restoration aims to recover the clean image $\mathcal{X}$ from the degraded observation $\mathcal{Y}$ [15, 77], modeled as:

$$\mathcal{Y} = \mathcal{H}(\mathcal{X}) + \mathcal{N}, \tag{1}$$

where $\mathcal{H}$ represents multiplicative degradation operations and $\mathcal{N}$ denotes additive degradation operators. For the denoising task, $\mathcal{H}$ is an identity operation. For the deblurring task, $\mathcal{H}$ represents the blurring operation. For the inpainting task, $\mathcal{H}$ denotes a binary mask. In practice, the specific degradation in HSI often involves a combination of unknown multiplicative and additive operators. Without prior knowledge of the degradation type, selecting and deploying a specific restoration method requires maintaining multiple specialized models, inevitably leading to high storage costs and complex model management.

3.2. Overall Pipeline

Given the degraded observation $\mathcal{Y} \in \mathbb{R}^{H \times W \times B}$, where $H \times W$ represents the spatial resolution and B denotes the number of spectral bands, MP-HSIR first applies a single-layer convolution to extract shallow features. As illustrated in Figure 11 (a), these features are processed through a three-level hierarchical encoder with downsampling operations. This process reduces spatial resolution while increasing channel capacity to obtain multi-scale deep features $F_l^e \in \mathbb{R}^{H \times W \times C}$, where C is the number of channels. Each encoder-decoder pair consists of multiple Prompt-Guided Spatial-Spectral Transformer Blocks (PGSSTBs), with the number of blocks progressively increasing at deeper levels.

To integrate degradation information into the decoding process, we introduce the Text-Visual Synergistic Prompt (TVSP) module at each skip connection between the encoder and decoder. The TVSP module leverages textual and visual prompts to incorporate semantic guidance and fine-grained details, effectively capturing degradation characteristics for restoration. Finally, the restored HSI is generated via a 3×3 convolution layer followed by an image-level residual connection. The following sections detail the designs of the PGSSTB and TVSP modules.

3.3. Prompt-Guided Spatial-Spectral Transformer

The PGSSTB is the core component of MP-HSIR, integrating Spatial Self-Attention (SSA), Prompt-Guided Spectral
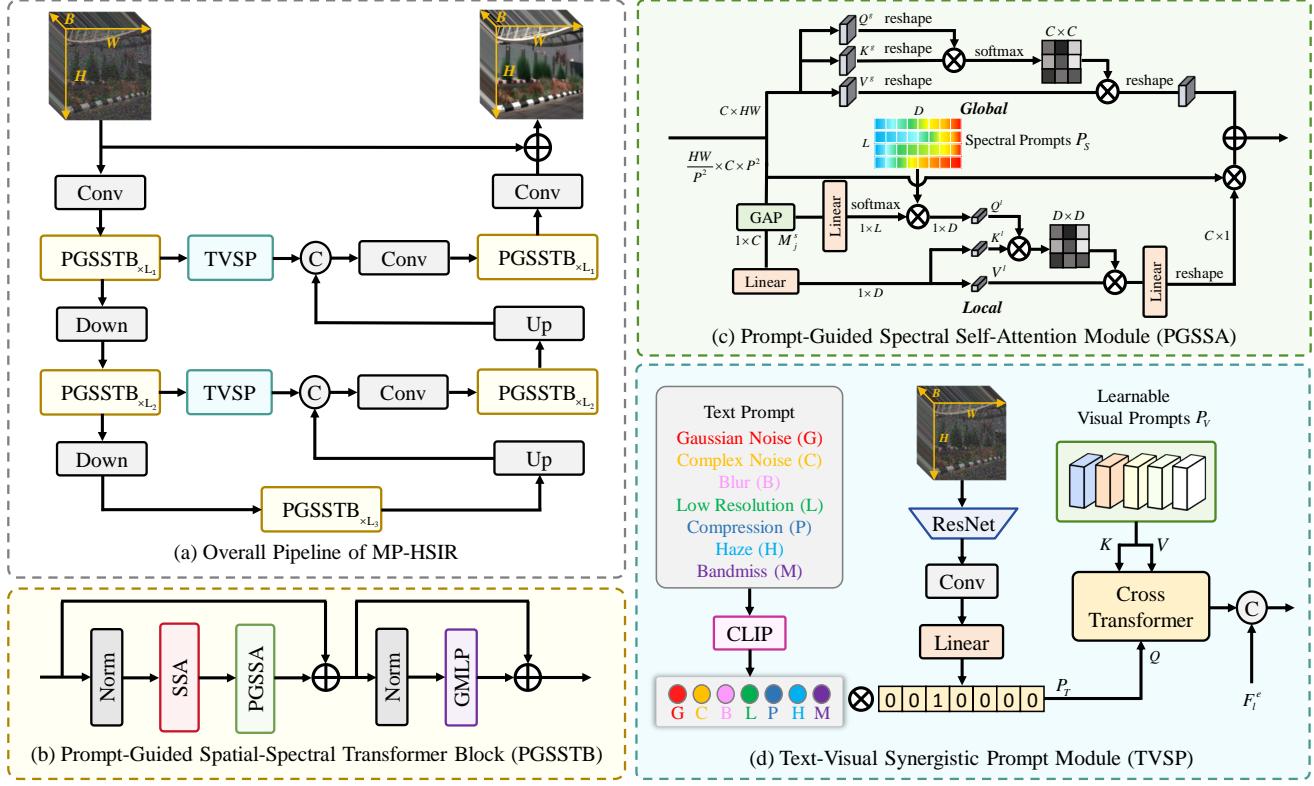
Figure 3. (a) The architecture of the proposed MP-HSIR. (b) Prompt-Guided Spatial-Spectral Transformer Block (PGSSTB). (c) Design of the Prompt-Guided Spectral Self-Attention (PGSSA) Module. (d) Text-Visual Synergistic Prompt (TVSP) Module.

Self-Attention (PGSSA), and a gated multi-layer perceptron (GMLP) [38]. To enhance training stability and convergence speed, layer normalization and skip connections [20] are incorporated, as shown in Figure 11 (b). SSA computes attention along the spatial dimension, capturing the non-local similarity in HSI. To improve computational efficiency while preserving the ability to model long-range dependencies, a sliding window [40] of size $P \times P$ is adopted.

While SSA captures spatial dependencies, spectral self-attention models long-range correlations across spectral bands, which is crucial for exploiting HSI's rich spectral information. To compute spectral similarity, the input features are transposed and reshaped into $F^{in} \in \mathbb{R}^{C \times HW}$ and processed through two complementary branches: global spectral self-attention and prompt-guided local spectral self-attention. The outputs from both branches are then fused and selectively refined using a GMLP. The following sections detail the two branches of PGSSA.

Global Spectral Self-Attention. Global spectral self-attention captures inter-channel dependencies across the entire HSI, as illustrated in the upper part of Figure 11 (c). Specifically, the input feature F^{in} is first projected into the *query* $Q^g \in \mathbb{R}^{C \times HW}$, *key* $K^g \in \mathbb{R}^{C \times HW}$, and *value* $V^g \in \mathbb{R}^{C \times HW}$ using 1×1 point-wise convolutions W^P,

followed by 3×3 depth-wise convolutions W^D:

$$[Q^g, K^g, V^g] = W^D W^P \left[F^{in}, F^{in}, F^{in} \right]. \quad (2)$$

To capture diverse spectral relationships across different bands, we further divide Q^g, K^g, and V^g into multiple heads. Within each head, the global spectral attention map $A^g \in \mathbb{R}^{C \times C}$ is computed using the element-wise dot product between Q^g and K^g, formulated as:

$$A^g = \text{Softmax} \left(\frac{Q^g \cdot K^g}{\epsilon} \right),$$
$$\text{Attention} \left(Q^g, K^g, V^g \right) = W^P \left(A^g V^g \right), \quad (3)$$

where ϵ is a learnable scaling factor that normalizes the results of the dot product.

Prompt-Guided Local Spectral Self-Attention. Unlike global spectral self-attention, local spectral self-attention models spectral channel dependencies within localized spatial regions, as illustrated in the lower part of Figure 11 (c). Specifically, the input feature F^{in} is divided into $\frac{HW}{P^2}$ non-overlapping local patches $\{M_1^{in}, M_2^{in}, \ldots, M_J^{in}\}$, where each patch $M_j^{in} \in \mathbb{R}^{C \times P^2}$ has the same spatial size as the spatial self-attention window. To extract representative spectral features $M_j^s \in \mathbb{R}^{1 \times C}$ from each patch, global average

pooling is applied along the spatial dimension:

$$M_j^s = \left(\text{AvgPool} \left(M_j^{in} \right) \right)^\top. \qquad (4)$$

However, due to the susceptibility of spectral structures to various degradations, purely local modeling may lead to an overly dispersed attention distribution, preventing the model from focusing on the most informative spectral channels. To address this, a learnable spectral prompt, $P_S \in \mathbb{R}^{L \times D}$, is introduced to guide the attention mechanism toward essential spectral patterns, where L denotes the number of universal low-rank spectral patterns in P_S, and D represents the dimension. Specifically, M_j^s undergoes a linear transformation followed by Softmax normalization to produce weights. These weights are then used to compute a weighted sum of P_S, which is subsequently projected to obtain the query Q^l. Meanwhile, M_j^s is projected into the same low-dimensional space and further transformed to generate the key K^l and value V^l, formulated as:

$$\begin{aligned} Q^l &= \text{Softmax} \left(M_j^s W_1^l \right) P_S W_3^l, \\ \left[K^l, V^l \right] &= M_j^s W_2^l W_3^l, \end{aligned} \qquad (5)$$

where the linear layer weights W_1^l, W_2^l, and W_3^l have dimensions $C \times L$, $C \times D$, and $D \times D$, respectively.

The spectral prompt P_S, learned during training, provides universally applicable low-rank spectral patterns for local spectral self-attention, enabling any local spectral feature to be represented as a linear combination of these patterns. This enhances the performance of local spectral modeling and facilitates spectral information recovery, thereby improving the model's generalization across different datasets and degradation scenarios. Finally, the local spectral attention map $A^l \in \mathbb{R}^{D \times D}$ can be obtained by:

$$\begin{aligned} A^l &= \text{Softmax} \left(\frac{Q^l \cdot K^l}{\epsilon} \right), \\ \text{Attention} \left(Q^l, K^l, V^l \right) &= W^P \left(A^l V^l \right), \end{aligned} \qquad (6)$$

where W^P remaps the low-dimensional spectral features to the original dimension $M_j^{out} \in \mathbb{R}^{C \times 1}$, which is then used to weight M_j^{in} to obtain the final output.

3.4. Text-Visual Synergistic Prompt

The spectral prompt exhibits strong robustness to HSIs with varying degradations but lacks explicit guidance on the degradation type. To address this limitation, we introduce the TVSP module, as illustrated in Figure 11 (d), which integrates textual prompts and learnable visual prompts to provide degradation-specific information for the restoration network.

First, we employ a degradation predictor Φ [11] to classify the degradation type of the input observation (details are provided in Section A of the supplementary material). Based on predefined textual descriptions T_{text} corresponding to different degradation types, a frozen CLIP model [55] generates embeddings that serve as the textual prompt P_T. To bridge the domain gap between RGB and HSI, these embeddings are transformed into learnable parameters, enabling the network to adapt and refine the textual prompts during training for improved alignment with HSI characteristics. The final textual prompt is selected based on the classification result:

$$P_T = \Phi(\mathcal{X}) \cdot \text{Clip} \left(T_{text} \right). \qquad (7)$$

However, the textual prompt P_T provides only global degradation information and lacks pixel-level precision. To address this, we introduce a learnable visual prompt P_V and fuse it with the textual prompt via a cross-attention. This allows P_T to regulate global degradation while P_V refines local features, enabling degradation information to be effectively integrated and adjusted, formally expressed as:

$$F_l^{out} = \text{Concat} \left(F_l^e, \text{Attention} \left(P_T, P_V \right) \right), \qquad (8)$$

where the output F_l^{out} is finally passed to the decoder via a skip connection. Compared to VLM-based dual prompts, TVSP is more flexible and adaptive, enabling prompt adjustments for different HSI domains.

4. Experiments

4.1. Experimental setup

Datasets. We employ 13 hyperspectral datasets for training and testing, comprising two natural scene HSI datasets and 11 remote sensing HSI datasets. The natural scene datasets include ICVL [3] and ARAD [4], while the remote sensing datasets consist of Xiong'an [72], WDC [81], Pavia City and Pavia University [24], Houston [66], Chikusei [73], Eagle [51], Berlin [49], APEX [25], Urban [5], and 10 EO-1 Hyperion scenes collected in this study. For the natural scene HSI datasets, 1,000 images are cropped into 64×64×31 patches for training, while an additional 100 non-overlapping images are reserved for testing. For the first eight remote sensing datasets, 80% of each image is cropped into 64×64×100 patches for training, with the remaining regions used for testing. The last three remote sensing datasets are designated for real-world experiments. Due to the substantial domain differences between natural scenes and remote sensing data, we train models separately on each dataset category. To ensure a comprehensive evaluation, multiple test datasets are randomly assigned to each task, ensuring that both natural scene and remote sensing HSI datasets are included in every task. Moreover, normalization is conducted on all datasets. A detailed description of the datasets is provided in Section B of the supplementary material.

Settings. To validate the effectiveness and generalization capability of the proposed model, we conducted evaluations

Type	Method	Gaussian Denoising (Sigma = 30, 50, 70)			Method	Complex Denoising (Case = 1, 2, 3, 4)		
		ICVL [3]	ARAD [4]	Xiong'an [72]		ICVL [3]	ARAD [4]	WDC [81]
		PSNR / SSIM ↑	PSNR / SSIM ↑	PSNR / SSIM ↑		PSNR / SSIM ↑	PSNR / SSIM ↑	PSNR / SSIM ↑
Task Specific	QRNN3D [63]	39.99 / 0.947	39.18 / 0.932	36.06 / 0.829	QRNN3D [63]	41.60 / 0.966	41.11 / 0.960	30.82 / 0.868
	SST [33]	41.31 / 0.959	40.86 / 0.955	37.53 / 0.850	SST [33]	42.43 / 0.971	41.95 / 0.967	32.71 / 0.889
	SERT [34]	41.55 / 0.967	41.09 / 0.959	37.83 / 0.859	SERT [34]	43.31 / 0.976	42.87 / 0.973	33.31 / 0.903
	LDERT [35]	41.92 / 0.969	41.47 / 0.965	38.14 / 0.865	LDERT [35]	43.42 / 0.977	43.02 / 0.974	33.49 / 0.904
All in One	AirNet [32]	39.76 / 0.943	39.19 / 0.920	31.94 / 0.668	AirNet [32]	40.68 / 0.959	40.09 / 0.945	28.07 / 0.726
	PromptIR [52]	40.25 / 0.953	39.69 / 0.945	32.99 / 0.684	PromptIR [52]	41.29 / 0.965	40.71 / 0.954	28.83 / 0.735
	PIP [36]	40.87 / 0.958	40.25 / 0.952	32.64 / 0.674	PIP [36]	41.67 / 0.968	41.17 / 0.962	28.50 / 0.724
	HAIR [7]	40.51 / 0.956	39.91 / 0.949	32.54 / 0.679	HAIR [7]	40.63 / 0.958	40.15 / 0.947	28.18 / 0.729
	InstructIR [12]	41.02 / 0.960	40.32 / 0.954	31.74 / 0.666	InstructIR [12]	40.12 / 0.957	39.81 / 0.952	27.49 / 0.707
	PromptHSI [30]	40.65 / 0.960	40.04 / 0.956	38.07 / 0.881	PromptHSI [30]	39.14 / 0.955	38.75 / 0.936	33.77 / 0.912
	MP-HSIR (Ours)	41.62 / 0.964	41.09 / 0.960	38.81 / 0.897	MP-HSIR (Ours)	42.29 / 0.971	41.99 / 0.969	34.07 / 0.918

Type	Method	Gaussian Deblurring (Radius = 9, 15, 21 & 7, 11, 15)			Method	Super-Resolution (Scale = 2, 4, 8)		
		ICVL [3]	PaviaC [24]	Eagle [51]		ARAD [4]	PaviaU [24]	Houston [66]
		PSNR / SSIM ↑	PSNR / SSIM ↑	PSNR / SSIM ↑		PSNR / SSIM ↑	PSNR / SSIM ↑	PSNR / SSIM ↑
Task Specific	Stripformer [58]	46.03 / 0.988	37.13 / 0.913	41.96 / 0.958	SNLSR [23]	36.05 / 0.898	30.55 / 0.730	31.70 / 0.787
	FFTformer [27]	46.65 / 0.988	37.96 / 0.921	42.76 / 0.962	MAN [60]	36.88 / 0.911	30.92 / 0.733	32.03 / 0.791
	LoFormer [47]	47.15 / 0.989	37.72 / 0.917	42.59 / 0.962	ESSAformer [78]	37.40 / 0.918	31.34 / 0.738	32.37 / 0.793
	MLWNet [14]	47.66 / 0.990	39.01 / 0.928	44.04 / 0.969	SRFormer [80]	38.02 / 0.922	31.80 / 0.751	32.80 / 0.803
All in One	AirNet [32]	47.21 / 0.989	37.76 / 0.918	42.42 / 0.963	AirNet [32]	36.73 / 0.910	30.93 / 0.735	32.00 / 0.791
	PromptIR [52]	47.67 / 0.990	38.72 / 0.927	43.74 / 0.968	PromptIR [52]	37.37 / 0.918	31.53 / 0.746	32.73 / 0.799
	PIP [36]	47.52 / 0.990	38.52 / 0.924	43.17 / 0.967	PIP [36]	38.36 / 0.926	31.77 / 0.749	32.89 / 0.805
	HAIR [7]	46.45 / 0.988	37.93 / 0.919	42.77 / 0.964	HAIR [7]	36.84 / 0.915	31.47 / 0.745	32.54 / 0.796
	InstructIR [12]	34.05 / 0.798	27.03 / 0.602	32.68 / 0.766	InstructIR [12]	36.51 / 0.913	31.34 / 0.741	32.52 / 0.793
	PromptHSI [30]	32.52 / 0.817	36.73 / 0.912	39.75 / 0.954	PromptHSI [30]	35.03 / 0.904	30.75 / 0.732	31.85 / 0.775
	MP-HSIR (Ours)	48.07 / 0.990	39.00 / 0.927	43.72 / 0.968	MP-HSIR (Ours)	38.25 / 0.924	31.97 / 0.760	33.06 / 0.810

Method	Inpainting (Mask Rate = 0.7, 0.8, 0.9)		Method	Dehazing (Omega = 0.5, 0.75, 1)		Method	Completion (Rate = 0.1, 0.2 0.3)	
	ICVL [3]	Chikusei [73]		PaviaU [24]	Eagle [51]		ARAD [4]	Berlin [49]
	PSNR / SSIM ↑	PSNR / SSIM ↑		PSNR / SSIM ↑	PSNR / SSIM ↑		PSNR / SSIM ↑	PSNR / SSIM ↑
NAFNet [8]	44.39 / 0.987	39.82 / 0.953	SGNet [45]	34.28 / 0.963	37.22 / 0.976	NAFNet [8]	47.04 / 0.995	38.35 / 0.907
Restormer [76]	45.79 / 0.990	36.33 / 0.899	SCANet [18]	36.59 / 0.978	39.64 / 0.985	Restormer [76]	48.34 / 0.995	35.07 / 0.606
DDS2M [48]	42.18 / 0.969	34.94 / 0.887	MB-Taylor [54]	37.99 / 0.983	41.03 / 0.991	SwinIR [37]	49.75 / 0.995	35.45 / 0.886
HIR-Diff [50]	38.91 / 0.949	37.65 / 0.916	DCMPNet [79]	37.20 / 0.985	40.24 / 0.990	MambaIR [16]	50.26 / 0.995	36.12 / 0.888
AirNet [32]	42.60 / 0.981	37.46 / 0.919	AirNet [32]	35.59 / 0.965	38.83 / 0.981	AirNet [32]	45.27 / 0.992	35.91 / 0.624
PromptIR [52]	46.38 / 0.990	38.07 / 0.930	PromptIR [52]	37.41 / 0.982	40.73 / 0.992	PromptIR [52]	46.60 / 0.994	40.45 / 0.652
PIP [36]	43.37 / 0.982	38.43 / 0.930	PIP [36]	37.62 / 0.982	40.74 / 0.990	PIP [36]	47.36 / 0.993	37.20 / 0.668
HAIR [7]	44.02 / 0.982	38.05 / 0.927	HAIR [7]	36.76 / 0.978	40.86 / 0.992	HAIR [7]	45.08 / 0.992	38.01 / 0.650
InstructIR [12]	44.07 / 0.986	36.11 / 0.907	InstructIR [12]	34.72 / 0.971	37.65 / 0.982	InstructIR [12]	51.31 / 0.997	35.97 / 0.580
PromptHSI [30]	41.48 / 0.972	37.33 / 0.946	PromptHSI [30]	36.77 / 0.974	39.78 / 0.984	PromptHSI [30]	47.34 / 0.994	43.36 / 0.972
MP-HSIR (Ours)	51.53 / 0.996	43.63 / 0.979	MP-HSIR (Ours)	39.59 / 0.986	42.41 / 0.995	MP-HSIR (Ours)	56.48 / 0.999	49.50 / 0.987

Table 1. **[All-in-one]** Quantitative comparison of all-in-one and state-of-the-art task-specific methods on 7 HSI restoration tasks. The best and second-best performances are highlighted in red and blue, respectively.

under three different settings. **(1) All-in-one:** A unified model was trained on seven HSI restoration tasks, including Gaussian denoising, complex denoising, Gaussian deblurring, super-resolution, inpainting, dehazing, and band completion. **(2) Generalization:** Few-shot and zero-shot learning were performed on unseen tasks. Motion deblurring was evaluated after fine-tuning, while Poisson denoising was assessed directly using the pre-trained model. **(3) Real-World:** For real-world denoising, following the settings of [33], the model was fine-tuned on the APEX dataset [25] and evaluated on the Urban dataset [5]. For real-world dehazing, the model was directly evaluated on the EO-1 Hyperion data. Detailed experimental settings for each task, including degradation synthesis models and intensity ranges, are provided

in Section C of the supplementary material.

Implementation Details. Due to the difference in data volume, we employed distinct training strategies for natural scene and remote sensing HSI datasets. Both utilized the AdamW optimizer ($\beta_1 = 0.9, \beta_2 = 0.999$) with L1 loss and a batch size of 32. For natural HSIs, training was conducted for 100 epochs with an initial learning rate of 2×10^{-4}, which was gradually reduced to 1×10^{-6} using cosine annealing [41]. In contrast, for remote sensing HSIs, the initial learning rate was set to 1×10^{-4}, and training was extended to 300 epochs. Given the higher spectral dimensionality of remote sensing HSIs, the width of the all-in-one model was increased by a factor of 1.5, while task-specific models were fine-tuned to achieve optimal performance.
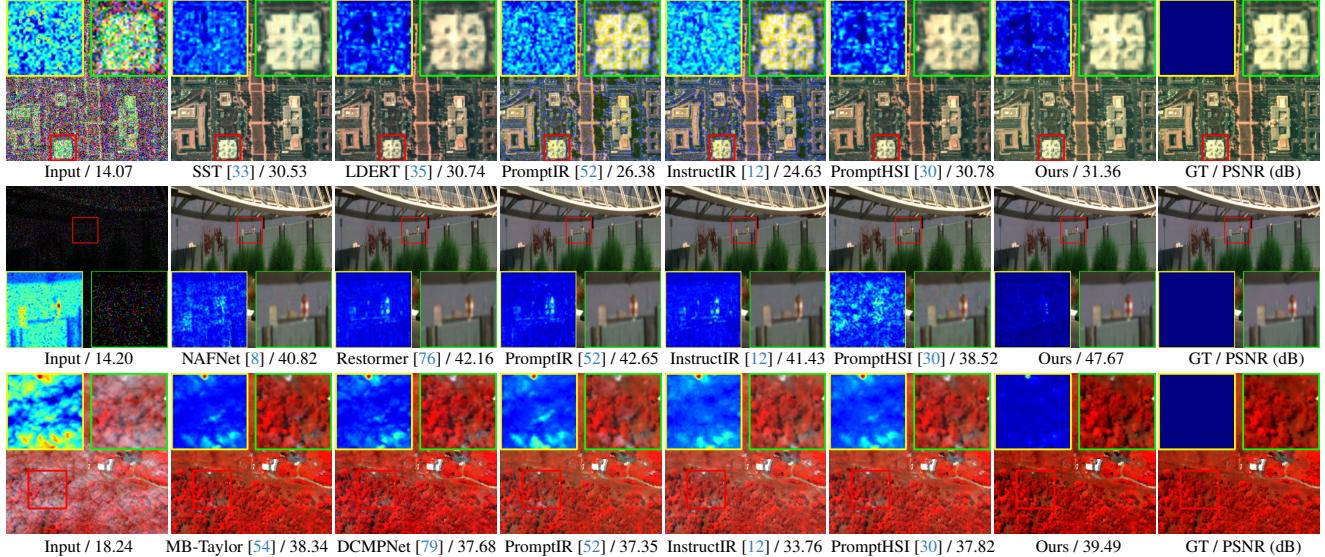
Figure 4. **[All-in-one]** Visual comparison results on *complex denoising*, *inpainting*, and *dehazing*. The zoomed-in regions are highlighted with red boxes, the corresponding zoomed results are marked with green boxes, and the residual maps are outlined with yellow boxes.
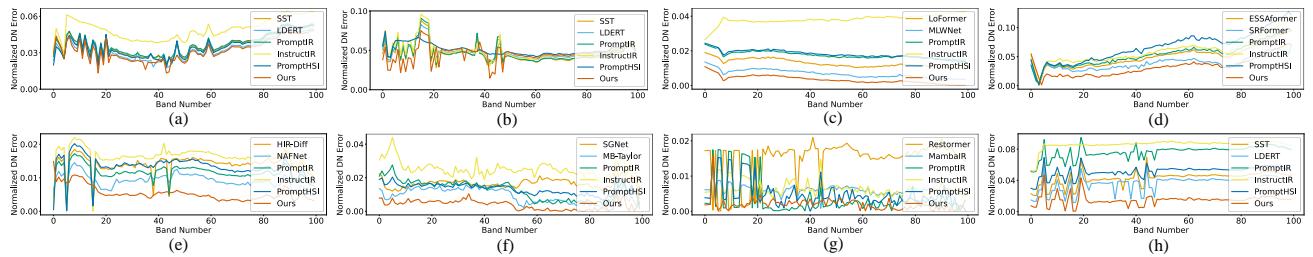

Figure 5. The spectral errors of the restored HSIs across multiple tasks. (a) *Gaussian denoising*. (b) *Complex denoising*. (c) *Gaussian deblurring*. (d) *Super-resolution*. (e) *Inpainting*. (f) *Dehazing*. (g) *Band completion*. (h) *Poisson denoising*. Zoom in for the best view.

Type	Method	Motion Deblurring		Methods	Poisson Denoising	
		PSNR ↑	SSIM ↑		PSNR ↑	SSIM ↑
Task Specific	Stripformer [58]	37.91	0.948	QRNN3D [63]	35.98	0.910
	FFTformer [27]	38.42	0.950	SST [33]	37.51	0.914
	LoFormer [47]	38.94	0.953	SERT [34]	37.46	0.913
	MLWNet [14]	39.28	0.959	LDERT [35]	37.92	0.915
All in One	AirNet [32]	37.43	0.947	AirNet [32]	33.91	0.896
	PromptIR [52]	38.77	0.951	PromptIR [52]	34.83	0.902
	PIP [36]	38.55	0.950	PIP [36]	34.52	0.901
	HAIR [7]	37.58	0.948	HAIR [7]	33.88	0.901
	InstructIR [12]	36.58	0.942	InstructIR [12]	33.96	0.895
	PromptHSI [30]	36.79	0.945	PromptHSI [30]	37.25	0.912
	MP-HSIR (Ours)	40.06	0.965	MP-HSIR (Ours)	38.56	0.922

Table 2. **[Generalization]** The results of *motion deblurring* on the ICVL dataset [3] and *Poisson denoising* on the Houston dataset [66]. Task-specific methods are trained on the entire dataset, while all-in-one methods are fine-tuned using only 5% of the data.

Evaluation Metrics and Comparisons Methods. We employed PSNR and SSIM [61] as quantitative metrics for evaluation. The comparison methods included six all-in-one models, *i.e.*, AirNet [32], PromptIR [52], PIP [36], HAIR [7], InstructIR [12], and PromptHSI [30], along with 22 state-of-the-art task-specific models.

4.2. Comparison with state-of-the-art methods

All-in-one. Table 1 presents the quantitative performance of seven all-in-one methods and 22 task-specific approaches across seven HSI restoration tasks. Our method consistently outperforms all all-in-one methods and surpasses state-of-the-art task-specific approaches in multiple tasks, achieving significant PSNR improvements in inpainting, dehazing, and band completion. Furthermore, our method attains the best or near-best performance across all hyperspectral remote sensing datasets. Notably, InstructIR and PromptHSI exhibit anomalous results in the deblurring task due to their inability to effectively distinguish different types of HSI degradation. Visualization comparison of prompts is provided in Section D of the supplementary material.

Figure 9 presents visual comparisons for complex denoising, inpainting, and dehazing. The residual maps highlight the superiority of our method in structural recovery and fine-detail reconstruction. Figure 12 illustrates the normalized digital number (DN) error between the restored and ground truth images across spectral bands. Leveraging spectral prompts, our method achieves the most accurate spectral
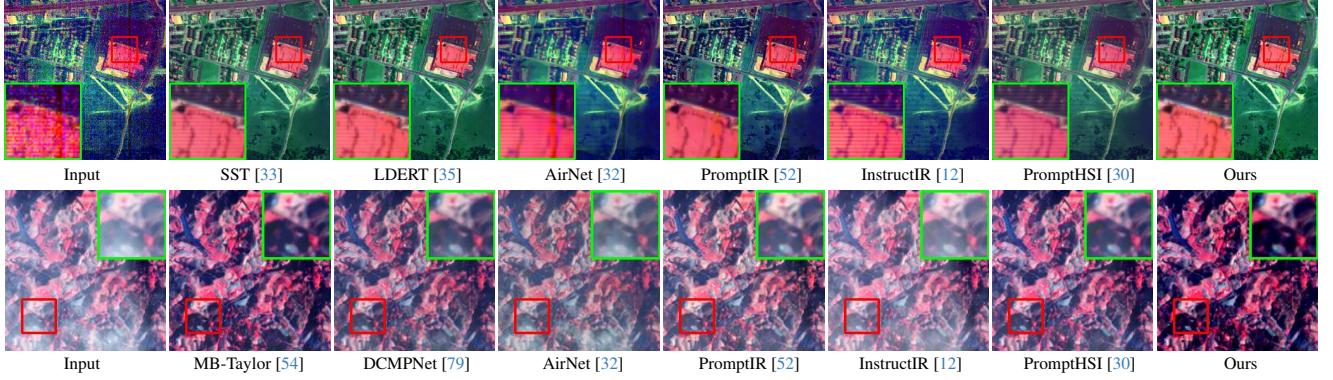
Figure 6. **[Real-world]** Visual comparison results on *real denoising* and *real dehazing*. Zoom in for the best view.

Method	PSNR ↑	SSIM ↑	Params (M)
Baseline (Only Spatial SA)	39.24	0.963	20.93
+ Textual Prompt P_T	39.62	0.964	21.51
+ Visual Prompt P_V	39.57	0.964	23.68
+ Textual Prompt P_T + Visual Prompt P_V	39.90	0.964	24.26
+ Global Spectral SA + P_T + P_T	40.63	0.969	30.07
+ Local Spectral SA + P_T + P_V	40.46	0.968	24.43
+ Local Spectral SA + P_T + P_V + Spectral Prompt P_S	41.05	0.971	25.10
Full Model	**41.98**	**0.974**	30.91

Table 3. Ablation study to verify the effectiveness of modules on Chikusei dataset in *inpainting* task with mask ratio = 0.9.

Figure 7. Visualization of the activation proportions for universal low-rank spectral patterns within the spectral prompt.

reconstruction across all tasks.

Generalization. Table 2 presents the experimental results for motion blur removal using few-shot learning and Poisson noise removal using zero-shot learning. The proposed method exhibits superior generalization ability compared to existing approaches under both learning paradigms.

Real-world. As shown in Figure 13, we present a comparative visualization of all-in-one and task-specific methods applied to real-world denoising and dehazing scenarios. The results highlight the proposed method's effectiveness in restoring texture details and spectral structure, while mitigating common artifacts like over-smoothing and spectral distortion.

Additional Results. More quantitative results and visualizations are in Section E of the supplementary material.

4.3. Model Analysis

Ablation Study. To assess the effectiveness of each module in the proposed MP-HSIR framework, we conducted an ablation study, starting with a baseline model that includes only spatial self-attention (SA) and then progressively incorporating textual prompts P_T, learnable visual prompts P_V, global spectral self-attention, local spectral self-attention, and spectral prompts P_S. As shown in Table 3, both accuracy metrics for the inpainting task on the Chikusei dataset progressively improve with the addition of each module. Notably, the local spectral self-attention module guided by
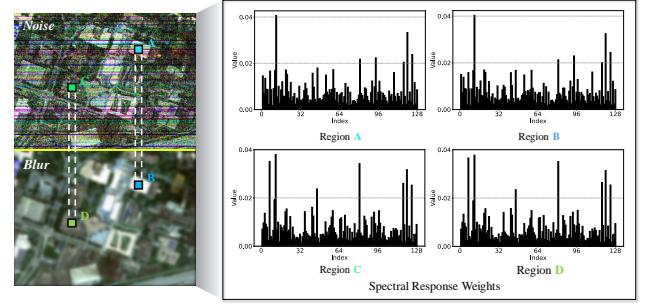
spectral prompts provides the most significant performance gain, attributed to the additional spectral guidance offered by spectral prompts. Results for other tasks are provided in Section E of the supplementary material.

Visualization of Spectral Prompt. To further investigate the role of spectral prompts, we visualize the activation distribution of universal low-rank spectral patterns under both noise and blur degradations in Figure 14. By selecting identical regions from both degraded images for comparison, we observe that despite different degradation types, the activation patterns remain highly consistent within the same regions. This indicates that spectral prompts effectively capture key spectral information in HSI and demonstrate strong robustness against different types of degradation.

5. Conclusion

HSI restoration is challenging due to diverse and often unknown degradation types, while existing methods are typically limited to specific degradation scenarios. In this work, we propose MP-HSIR, a universal HSI restoration framework that integrates spectral, textual, and visual prompts. MP-HSIR introduces a novel prompt-guided spatial-spectral transformer, where spectral prompts provide universal low-rank spectral patterns to enhance spectral reconstruction. Furthermore, the text-visual synergistic prompts combine high-level semantic representations with fine-grained visual

features to guide degradation modeling. Extensive experiments on 9 HSI restoration tasks—including all-in-one restoration, generalization testing, and real-world scenarios—demonstrate the superior robustness and adaptability of MP-HSIR under diverse degradation conditions.

References

[1] Yuang Ai, Huaibo Huang, Xiaoqiang Zhou, Jiexiang Wang, and Ran He. Multimodal prompt perceiver: Empower adaptiveness generalizability and fidelity for all-in-one image restoration. In *Proceedings of the IEEE/CVF Conference on Computer Vision and Pattern Recognition*, pages 25432–25444, 2024. 1, 2, 3

[2] Margaret E Andrew and Susan L Ustin. The role of environmental context in mapping invasive plants with hyperspectral image data. *Remote Sensing of Environment*, 112(12):4301–4317, 2008. 1

[3] Boaz Arad and Ohad Ben-Shahar. Sparse recovery of hyperspectral signal from natural rgb images. In *Computer Vision–ECCV 2016: 14th European Conference, Amsterdam, the Netherlands, October 11–14, 2016, Proceedings, Part VII 14*, pages 19–34. Springer, 2016. 5, 6, 7, 13, 15, 16, 17

[4] Boaz Arad, Radu Timofte, Rony Yahel, Nimrod Morag, Amir Bernat, Yuanhao Cai, Jing Lin, Zudi Lin, Haoqian Wang, Yulun Zhang, et al. Ntire 2022 spectral recovery challenge and data set. In *Proceedings of the IEEE/CVF Conference on Computer Vision and Pattern Recognition*, pages 863–881, 2022. 5, 6, 13, 15, 16, 17

[5] M. F. Baumgardner, L. L. Biehl, and D. A. Landgrebe. 220-band aviris hyperspectral image data set: June 12, 1992 indian pine test site 3, 2015. Available: https://purr.purdue.edu/publications/1947/1. 5, 6, 13

[6] Théo Bodrito, Alexandre Zouaoui, Jocelyn Chanussot, and Julien Mairal. A trainable spectral-spatial sparse coding model for hyperspectral image restoration. *Advances in Neural Information Processing Systems*, 34:5430–5442, 2021. 3

[7] Jin Cao, Yi Cao, Li Pang, Deyu Meng, and Xiangyong Cao. Hair: Hypernetworks-based all-in-one image restoration. *arXiv preprint arXiv:2408.08091*, 2024. 3, 6, 7, 15, 16, 17, 18

[8] Liangyu Chen, Xiaojie Chu, Xiangyu Zhang, and Jian Sun. Simple baselines for image restoration. In *European Conference on Computer Vision*, pages 17–33. Springer, 2022. 6, 7, 17

[9] Yong Chen, Wenzhen Lai, Wei He, Xi-Le Zhao, and Jinshan Zeng. Hyperspectral compressive snapshot reconstruction via coupled low-rank subspace representation and self-supervised deep network. *IEEE Transactions on Image Processing*, 33:926–941, 2024. 1

[10] Yurong Chen, Hui Zhang, Yaonan Wang, Yimin Yang, and Jonathan Wu. Flex-dld: Deep low-rank decomposition model with flexible priors for hyperspectral image denoising and restoration. *IEEE Transactions on Image Processing*, 33:1211–1226, 2024. 3

[11] Lu Chi, Borui Jiang, and Yadong Mu. Fast fourier convolution.

[12] Marcos V Conde, Gregor Geigle, and Radu Timofte. Instructir: High-quality image restoration following human instructions. In *European Conference on Computer Vision*, pages 1–21. Springer, 2024. 1, 2, 3, 6, 7, 8, 15, 16, 17, 18

[13] Mark A Folkman, Jay Pearlman, Lushalan B Liao, and Peter J Jarecke. Eo-1/hyperion hyperspectral imager design, development, characterization, and calibration. *Hyperspectral Remote Sensing of the Land and Atmosphere*, 4151:40–51, 2001. 13

[14] Xin Gao, Tianheng Qiu, Xinyu Zhang, Hanlin Bai, Kang Liu, Xuan Huang, Hu Wei, Guoying Zhang, and Huaping Liu. Efficient multi-scale network with learnable discrete wavelet transform for blind motion deblurring. In *Proceedings of the IEEE/CVF Conference on Computer Vision and Pattern Recognition*, pages 2733–2742, 2024. 6, 7, 16

[15] Pedram Ghamisi, Naoto Yokoya, Jun Li, Wenzhi Liao, Sicong Liu, Javier Plaza, Behnood Rasti, and Antonio Plaza. Advances in hyperspectral image and signal processing: A comprehensive overview of the state of the art. *IEEE Geoscience and Remote Sensing Magazine*, 5(4):37–78, 2017. 3

[16] Hang Guo, Jinmin Li, Tao Dai, Zhihao Ouyang, Xudong Ren, and Shu-Tao Xia. Mambair: A simple baseline for image restoration with state-space model. In *European Conference on Computer Vision*, pages 222–241. Springer, 2024. 6, 17

[17] Jianhua Guo, Jingyu Yang, Huanjing Yue, Hai Tan, Chunping Hou, and Kun Li. Rsdehazenet: Dehazing network with channel refinement for multispectral remote sensing images. *IEEE Transactions on Geoscience and Remote Sensing*, 59 (3):2535–2549, 2020. 14

[18] Yu Guo, Yuan Gao, Wen Liu, Yuxu Lu, Jingxiang Qu, Shengfeng He, and Wenqi Ren. Scanet: Self-paced semi-curricular attention network for non-homogeneous image dehazing. In *Proceedings of the IEEE/CVF Conference on Computer Vision and Pattern Recognition*, pages 1885–1894, 2023. 6, 17

[19] Yu Guo, Yuan Gao, Yuxu Lu, Huilin Zhu, Ryan Wen Liu, and Shengfeng He. Onerestore: A universal restoration framework for composite degradation. In *European Conference on Computer Vision*, pages 255–272. Springer, 2024. 1, 2

[20] Kaiming He, Xiangyu Zhang, Shaoqing Ren, and Jian Sun. Identity mappings in deep residual networks. In *Computer Vision–ECCV 2016: 14th European Conference, Amsterdam, The Netherlands, October 11–14, 2016, Proceedings, Part IV 14*, pages 630–645. Springer, 2016. 4

[21] Wei He, Quanming Yao, Chao Li, Naoto Yokoya, and Qibin Zhao. Non-local meets global: An integrated paradigm for hyperspectral denoising. In *Proceedings of the IEEE/CVF Conference on Computer Vision and Pattern Recognition*, pages 6868–6877, 2019. 1, 3

[22] Uta Heiden, Wieke Heldens, Sigrid Roessner, Karl Segl, Thomas Esch, and Andreas Mueller. Urban structure type characterization using hyperspectral remote sensing and height information. *Landscape and urban Planning*, 105 (4):361–375, 2012. 1

[23] Qian Hu, Xinya Wang, Junjun Jiang, Xiao-Ping Zhang, and Jiayi Ma. Exploring the spectral prior for hyperspectral image

Advances in Neural Information Processing Systems, 33:4479–4488, 2020. 5, 13

super-resolution. *IEEE Transactions on Image Processing*, 2024. 6, 16

[24] Xin Huang and Liangpei Zhang. A comparative study of spatial approaches for urban mapping using hyperspectral rosis images over pavia city, northern italy. *International Journal of Remote Sensing*, 30(12):3205–3221, 2009. 5, 6, 13, 16, 17

[25] Klaus I Itten, Francesco Dell'Endice, Andreas Hueni, Mathias Kneubühler, Daniel Schläpfer, Daniel Odermatt, Felix Seidel, Silvia Huber, Jürg Schopfer, Tobias Kellenberger, et al. Apex-the hyperspectral esa airborne prism experiment. *Sensors*, 8 (10):6235–6259, 2008. 5, 6, 13

[26] Junjun Jiang, Zengyuan Zuo, Gang Wu, Kui Jiang, and Xianming Liu. A survey on all-in-one image restoration: Taxonomy, evaluation and future trends. *arXiv preprint arXiv:2410.15067*, 2024. 1, 3

[27] Lingshun Kong, Jiangxin Dong, Jianjun Ge, Mingqiang Li, and Jinshan Pan. Efficient frequency domain-based transformers for high-quality image deblurring. In *Proceedings of the IEEE/CVF Conference on Computer Vision and Pattern Recognition*, pages 5886–5895, 2023. 6, 7, 16

[28] Yo-Yu Lai, Chia-Hsiang Lin, and Zi-Chao Leng. Hyper-restormer: A general hyperspectral image restoration transformer for remote sensing imaging. *arXiv preprint arXiv:2312.07016*, 2023. 3

[29] Zeqiang Lai, Chenggang Yan, and Ying Fu. Hybrid spectral denoising transformer with guided attention. In *Proceedings of the IEEE/CVF International Conference on Computer Vision*, pages 13065–13075, 2023. 3

[30] Chia-Ming Lee, Ching-Heng Cheng, Yu-Fan Lin, Yi-Ching Cheng, Wo-Ting Liao, Chih-Chung Hsu, Fu-En Yang, and Yu-Chiang Frank Wang. Prompthsi: Universal hyperspectral image restoration framework for composite degradation. *arXiv preprint arXiv:2411.15922*, 2024. 3, 6, 7, 8, 15, 16, 17, 18

[31] Yiming Lei, Jingqi Li, Zilong Li, Yuan Cao, and Hongming Shan. Prompt learning in computer vision: a survey. *Frontiers of Information Technology & Electronic Engineering*, 25(1): 42–63, 2024. 3

[32] Boyun Li, Xiao Liu, Peng Hu, Zhongqin Wu, Jiancheng Lv, and Xi Peng. All-in-one image restoration for unknown corruption. In *Proceedings of the IEEE/CVF Conference on Computer Vision and Pattern Recognition*, pages 17452–17462, 2022. 1, 3, 6, 7, 8, 15, 16, 17, 18

[33] Miaoyu Li, Ying Fu, and Yulun Zhang. Spatial-spectral transformer for hyperspectral image denoising. In *Proceedings of the AAAI Conference on Artificial Intelligence*, pages 1368–1376, 2023. 3, 6, 7, 8, 15

[34] Miaoyu Li, Ji Liu, Ying Fu, Yulun Zhang, and Dejing Dou. Spectral enhanced rectangle transformer for hyperspectral image denoising. In *Proceedings of the IEEE/CVF Conference on Computer Vision and Pattern Recognition*, pages 5805–5814, 2023. 3, 6, 7, 15

[35] Miaoyu Li, Ying Fu, Tao Zhang, Ji Liu, Dejing Dou, Chenggang Yan, and Yulun Zhang. Latent diffusion enhanced rectangle transformer for hyperspectral image restoration. *IEEE Transactions on Pattern Analysis and Machine Intelligence*, 2024. 1, 3, 6, 7, 8, 15

[36] Zilong Li, Yiming Lei, Chenglong Ma, Junping Zhang, and Hongming Shan. Prompt-in-prompt learning for universal image restoration. *arXiv preprint arXiv:2312.05038*, 2023. 2, 3, 6, 7, 15, 16, 17, 18

[37] Jingyun Liang, Jiezhang Cao, Guolei Sun, Kai Zhang, Luc Van Gool, and Radu Timofte. Swinir: Image restoration using swin transformer. In *Proceedings of the IEEE/CVF International Conference on Computer Vision*, pages 1833–1844, 2021. 6, 17

[38] Hanxiao Liu, Zihang Dai, David So, and Quoc V Le. Pay attention to mlps. *Advances in Neural Information Processing Systems*, 34:9204–9215, 2021. 4

[39] Yun-Yang Liu, Xi-Le Zhao, Yu-Bang Zheng, Tian-Hui Ma, and Hongyan Zhang. Hyperspectral image restoration by tensor fibered rank constrained optimization and plug-and-play regularization. *IEEE Transactions on Geoscience and Remote Sensing*, 60:1–17, 2021. 3

[40] Ze Liu, Yutong Lin, Yue Cao, Han Hu, Yixuan Wei, Zheng Zhang, Stephen Lin, and Baining Guo. Swin transformer: Hierarchical vision transformer using shifted windows. In *Proceedings of the IEEE/CVF International Conference on Computer Vision*, pages 10012–10022, 2021. 4

[41] Ilya Loshchilov and Frank Hutter. Sgdr: Stochastic gradient descent with warm restarts. *arXiv preprint arXiv:1608.03983*, 2016. 6, 13

[42] Bing Lu, Phuong D Dao, Jiangui Liu, Yuhong He, and Jiali Shang. Recent advances of hyperspectral imaging technology and applications in agriculture. *Remote Sensing*, 12(16):2659, 2020. 1

[43] Yuning Lu, Jianzhuang Liu, Yonggang Zhang, Yajing Liu, and Xinmei Tian. Prompt distribution learning. In *Proceedings of the IEEE/CVF Conference on Computer Vision and Pattern Recognition*, pages 5206–5215, 2022. 3

[44] Ziwei Luo, Fredrik K Gustafsson, Zheng Zhao, Jens Sjölund, and Thomas B Schön. Photo-realistic image restoration in the wild with controlled vision-language models. In *Proceedings of the IEEE/CVF Conference on Computer Vision and Pattern Recognition*, pages 6641–6651, 2024. 2, 3

[45] Xiaofeng Ma, Qunming Wang, and Xiaohua Tong. A spectral grouping-based deep learning model for haze removal of hyperspectral images. *ISPRS Journal of Photogrammetry and Remote Sensing*, 188:177–189, 2022. 3, 6, 17

[46] Matteo Maggioni, Vladimir Katkovnik, Karen Egiazarian, and Alessandro Foi. Nonlocal transform-domain filter for volumetric data denoising and reconstruction. *IEEE Transactions on Image Processing*, 22(1):119–133, 2012. 2

[47] Xintian Mao, Jiansheng Wang, Xingran Xie, Qingli Li, and Yan Wang. Loformer: Local frequency transformer for image deblurring. In *Proceedings of the 32nd ACM International Conference on Multimedia*, pages 10382–10391, 2024. 6, 7, 16

[48] Yuchun Miao, Lefei Zhang, Liangpei Zhang, and Dacheng Tao. Dds2m: Self-supervised denoising diffusion spatio-spectral model for hyperspectral image restoration. In *Proceedings of the IEEE/CVF International Conference on Computer Vision*, pages 12086–12096, 2023. 3, 6, 17

[49] Akpona Okujeni, Sebastian van der Linden, and Patrick Hostert. Berlin-urban-gradient dataset 2009: An enmap

preparatory flight campaign, 2016. Available: `https://doi.org/10.2312/enmap.2016.0021`. 5, 6, 13, 17

[50] Li Pang, Xiangyu Rui, Long Cui, Hongzhong Wang, Deyu Meng, and Xiangyong Cao. Hir-diff: Unsupervised hyperspectral image restoration via improved diffusion models. In *Proceedings of the IEEE/CVF Conference on Computer Vision and Pattern Recognition*, pages 3005–3014, 2024. 3, 6, 17

[51] Kabir Yunus Peerbhay, Onisimo Mutanga, and Riyad Ismail. Commercial tree species discrimination using airborne aisa eagle hyperspectral imagery and partial least squares discriminant analysis (pls-da) in kwazulu–natal, south africa. *ISPRS Journal of Photogrammetry and Remote Sensing*, 79:19–28, 2013. 5, 6, 13, 16, 17

[52] Vaishnav Potlapalli, Syed Waqas Zamir, Salman H Khan, and Fahad Shahbaz Khan. Promptir: Prompting for all-in-one image restoration. *Advances in Neural Information Processing Systems*, 36:71275–71293, 2023. 2, 3, 6, 7, 8, 15, 16, 17, 18

[53] Chenyang Qi, Zhengzhong Tu, Keren Ye, Mauricio Delbracio, Peyman Milanfar, Qifeng Chen, and Hossein Talebi. Spire: Semantic prompt-driven image restoration. In *European Conference on Computer Vision*, pages 446–464. Springer, 2024. 3

[54] Yuwei Qiu, Kaihao Zhang, Chenxi Wang, Wenhan Luo, Hongdong Li, and Zhi Jin. Mb-taylorformer: Multi-branch efficient transformer expanded by taylor formula for image dehazing. In *Proceedings of the IEEE/CVF International Conference on Computer Vision*, pages 12802–12813, 2023. 6, 7, 8, 17

[55] Alec Radford, Jong Wook Kim, Chris Hallacy, Aditya Ramesh, Gabriel Goh, Sandhini Agarwal, Girish Sastry, Amanda Askell, Pamela Mishkin, Jack Clark, et al. Learning transferable visual models from natural language supervision. In *International Conference on Machine Learning*, pages 8748–8763. PmLR, 2021. 5

[56] Lankapalli Ravikanth, Digvir S Jayas, Noel DG White, Paul G Fields, and Da-Wen Sun. Extraction of spectral information from hyperspectral data and application of hyperspectral imaging for food and agricultural products. *Food and Bioprocess Technology*, 10:1–33, 2017. 1

[57] Dunbin Shen, Jianjun Liu, Zebin Wu, Jinlong Yang, and Liang Xiao. Admm-hfnet: A matrix decomposition-based deep approach for hyperspectral image fusion. *IEEE Transactions on Geoscience and Remote Sensing*, 60:1–17, 2021. 3

[58] Fu-Jen Tsai, Yan-Tsung Peng, Yen-Yu Lin, Chung-Chi Tsai, and Chia-Wen Lin. Stripformer: Strip transformer for fast image deblurring. In *European Conference on Computer Vision*, pages 146–162. Springer, 2022. 6, 7, 16

[59] Yuting Wan, Xin Hu, Yanfei Zhong, Ailong Ma, Lifei Wei, and Liangpei Zhang. Tailings reservoir disaster and environmental monitoring using the uav-ground hyperspectral joint observation and processing: a case of study in xinjiang, the belt and road. In *IGARSS 2019-2019 IEEE International Geoscience and Remote Sensing Symposium*, pages 9713–9716. IEEE, 2019. 1

[60] Yan Wang, Yusen Li, Gang Wang, and Xiaoguang Liu. Multiscale attention network for single image super-resolution. In *Proceedings of the IEEE/CVF Conference on Computer Vision and Pattern Recognition*, pages 5950–5960, 2024. 6, 16

[61] Zhou Wang, Alan C Bovik, Hamid R Sheikh, and Eero P Simoncelli. Image quality assessment: from error visibility to structural similarity. *IEEE Transactions on Image Processing*, 13(4):600–612, 2004. 7

[62] Cody Weber, Rahim Aguejdad, Xavier Briottet, J Avala, Sophie Fabre, Jean Demuynck, Emmanuel Zenou, Yannick Deville, Moussa Sofiane Karoui, Fatima Zohra Benhalouche, et al. Hyperspectral imagery for environmental urban planning. In *IGARSS 2018-2018 IEEE International Geoscience and Remote Sensing Symposium*, pages 1628–1631. IEEE, 2018. 1

[63] Kaixuan Wei, Ying Fu, and Hua Huang. 3-d quasi-recurrent neural network for hyperspectral image denoising. *IEEE Transactions on Neural Networks and Learning Systems*, 32 (1):363–375, 2020. 1, 3, 6, 7, 15

[64] Chanyue Wu, Dong Wang, Yunpeng Bai, Hanyu Mao, Ying Li, and Qiang Shen. Hsr-diff: Hyperspectral image superresolution via conditional diffusion models. In *Proceedings of the IEEE/CVF International Conference on Computer Vision*, pages 7083–7093, 2023. 3

[65] Gang Wu, Junjun Jiang, Kui Jiang, and Xianming Liu. Harmony in diversity: Improving all-in-one image restoration via multi-task collaboration. In *Proceedings of the 32nd ACM International Conference on Multimedia*, pages 6015–6023, 2024. 1, 3

[66] Hao Wu and Saurabh Prasad. Convolutional recurrent neural networks for hyperspectral data classification. *Remote Sensing*, 9(3):298, 2017. 5, 6, 7, 13, 16

[67] Jiahua Xiao, Yang Liu, and Xing Wei. Region-aware sequence-to-sequence learning for hyperspectral denoising. In *European Conference on Computer Vision*, pages 218–235. Springer, 2024. 3

[68] Ting Xie, Shutao Li, and Jibao Lai. Adaptive rank and structured sparsity corrections for hyperspectral image restoration. *IEEE Transactions on Cybernetics*, 52(9):8729–8740, 2021. 3

[69] Meng Xu, Yanxin Peng, Ying Zhang, Xiuping Jia, and Sen Jia. Aacnet: Asymmetric attention convolution network for hyperspectral image dehazing. *IEEE Transactions on Geoscience and Remote Sensing*, 61:1–14, 2023. 1, 3

[70] Wei Xu, Qing Zhu, Na Qi, and Dongpan Chen. Deep sparse representation based image restoration with denoising prior. *IEEE Transactions on Circuits and Systems for Video Technology*, 32(10):6530–6542, 2022. 3

[71] Jingxiang Yang, Yong-Qiang Zhao, Chen Yi, and Jonathan Cheung-Wai Chan. No-reference hyperspectral image quality assessment via quality-sensitive features learning. *Remote Sensing*, 9(4):305, 2017. 15

[72] CEN Yi, Lifu Zhang, Xia Zhang, WANG Yueming, QI Wenchao, TANG Senlin, and Peng Zhang. Aerial hyperspectral remote sensing classification dataset of xiongan new area (matiwan village). *National Remote Sensing Bulletin*, 24(11): 1299–1306, 2020. 5, 6, 13, 15

[73] Naoto Yokoya and Akira Iwasaki. Airborne hyperspectral data over chikusei. *Space Appl. Lab., Univ. Tokyo, Tokyo, Japan, Tech. Rep. SAL-2016-05-27*, 5(5):5, 2016. 5, 6, 13, 17

[74] Dabing Yu, Qingwu Li, Xiaolin Wang, Zhiliang Zhang, Yixi Qian, and Chang Xu. Dstrans: Dual-stream transformer for hyperspectral image restoration. In *Proceedings of the IEEE/CVF Winter Conference on Applications of Computer Vision*, pages 3739–3749, 2023. 3

[75] Qiangqiang Yuan, Qiang Zhang, Jie Li, Huanfeng Shen, and Liangpei Zhang. Hyperspectral image denoising employing a spatial–spectral deep residual convolutional neural network. *IEEE Transactions on Geoscience and Remote Sensing*, 57 (2):1205–1218, 2018. 3

[76] Syed Waqas Zamir, Aditya Arora, Salman Khan, Munawar Hayat, Fahad Shahbaz Khan, and Ming-Hsuan Yang. Restormer: Efficient transformer for high-resolution image restoration. In *Proceedings of the IEEE/CVF Conference on Computer Vision and Pattern Recognition*, pages 5728–5739, 2022. 6, 7, 17

[77] Hongyan Zhang, Wei He, Liangpei Zhang, Huanfeng Shen, and Qiangqiang Yuan. Hyperspectral image restoration using low-rank matrix recovery. *IEEE Transactions on Geoscience and Remote Sensing*, 52(8):4729–4743, 2013. 3

[78] Mingjin Zhang, Chi Zhang, Qiming Zhang, Jie Guo, Xinbo Gao, and Jing Zhang. Essaformer: Efficient transformer for hyperspectral image super-resolution. In *Proceedings of the IEEE/CVF International Conference on Computer Vision*, pages 23073–23084, 2023. 1, 3, 6, 16

[79] Yafei Zhang, Shen Zhou, and Huafeng Li. Depth information assisted collaborative mutual promotion network for single image dehazing. In *Proceedings of the IEEE/CVF Conference on Computer Vision and Pattern Recognition*, pages 2846–2855, 2024. 6, 7, 8, 17

[80] Yupeng Zhou, Zhen Li, Chun-Le Guo, Song Bai, Ming-Ming Cheng, and Qibin Hou. Srformer: Permuted self-attention for single image super-resolution. In *Proceedings of the IEEE/CVF International Conference on Computer Vision*, pages 12780–12791, 2023. 6, 16

[81] Feiyun Zhu. Hyperspectral unmixing: ground truth labeling, datasets, benchmark performances and survey. *arXiv preprint arXiv:1708.05125*, 2017. 5, 6, 13, 15

Supplementary Materials

F. Degradation Preictor

The proposed universal multi-prompt framework, MP-HSIR, can perform specific restoration tasks either based on human instructions or autonomously via the degradation predictor. In this work, we employ a ResNet-34 network with fast Fourier convolution [11] to train classification models separately on natural scene and remote sensing hyperspectral datasets. The binary cross-entropy loss used for training is defined as follows:

$$\mathcal{L} = -\frac{1}{N} \sum_{i=1}^{N} \left[y_i \log p_i + (1 - y_i) \log (1 - p_i) \right], \quad (9)$$

where N denotes the number of samples, p_i represents the output after sigmoid activation, and y_i is the corresponding ground-truth label. The training was conducted with a batch size of 64, using the same optimizer as in the restoration experiments. The initial learning rate was set to 1×10^{-4} and progressively decreased to 1×10^{-6} via cosine annealing [41]. The model was trained for 1000 epochs on the natural scene hyperspectral dataset and 4000 epochs on the remote sensing hyperspectral dataset.

Table 4 presents the accuracy and precision of the degradation predictor for both hyperspectral datasets. The results show that the predictor achieves 100% accuracy and precision across all tasks, demonstrating MPIR-HSI's effectiveness in supporting all trained blind restoration tasks.

G. Dataset Details

This section provides a comprehensive overview of the 13 datasets used across 9 hyperspectral image (HSI) restoration tasks and real-world scenarios, as summarized in Table 5.

ARAD [4]. The ARAD dataset, derived from the NTIRE 2022 Spectral Recovery Challenge, was collected using a Specim IQ hyperspectral camera. It consists of 1,000 images, with 900 allocated for training and 50 for testing.

ICVL [3]. The ICVL dataset was obtained using a Specim PS Kappa DX4 hyperspectral camera combined with a rotating stage for spatial scanning. It contains 201 images, with 100 for training and 50 for testing, ensuring no scene overlap.

Xiong'an [72]. The Xiong'an dataset was captured using an imaging spectrometer developed by the Chinese Academy of Sciences. Three central regions of size 512 × 512 were randomly cropped for testing, while the remaining areas were used for training.

Task	Natural Scene		Remote Sensing	
	Accuracy ↑	Precision ↑	Accuracy ↑	Precision ↑
Gaussian Denoising	100.00	100.00	100.00	100.00
Complex Denoising	100.00	100.00	100.00	100.00
Gaussian Deblurring	100.00	100.00	100.00	100.00
Super-Resolution	100.00	100.00	100.00	100.00
Inpainting	100.00	100.00	100.00	100.00
Dehazing	100.00	100.00	100.00	100.00
Band Completion	100.00	100.00	100.00	100.00

Table 4. Accuracy and precision results of the degradation predictor in degradation classification

WDC [81]. The Washington DC (WDC) dataset was captured by a Hydice sensor. A central region of size 256 × 256 was selected for testing, with the remainder used for training.

PaviaC [24]. The Pavia Center (PaviaC) dataset was acquired using a ROSIS sensor, following the same partitioning strategy as the WDC dataset.

PaviaU [24]. The Pavia University (PaviaU) dataset was also collected using a ROSIS sensor, with the same partitioning strategy as WDC.

Houston [66]. The Houston dataset was obtained using an ITRES CASI-1500 sensor, employing the same partitioning strategy as WDC.

Chikusei [73]. The Chikusei dataset was captured using an HH-VNIR-C sensor. Four 512 × 512 regions were randomly cropped for testing, with the remaining areas used for training.

Eagle [51]. The Eagle dataset was collected using an AsiaEAGLE II sensor, following the same partitioning strategy as WDC.

Berlin [49]. The Berlin dataset utilizes only the HyMap image from the BerlinUrbGrad dataset. A 512 × 512 central region was randomly cropped for testing, while the remaining data were used for training.

Urban [5]. The Urban dataset, collected using a Hydice sensor, is specifically used for real-world denoising experiments.

APEX [25]. The APEX dataset exhibits characteristics similar to the Urban dataset and is primarily used for fine-tuning pre-trained models.

EO-1 [13]. The EO-1 dataset was captured by the Hyperion sensor. Ten scenes were collected for testing, with 67 invalid bands removed, retaining 175 valid bands for real-world dehazing experiments.

All datasets underwent min-max normalization, and training samples were uniformly cropped to 64 × 64.

Type	Dataset	Sensor	Wavelength (nm)	Channels	Size	GSD (m)
Natural HSIs	ARAD_1K	Specim IQ	400–700	31	482×512	/
	ICVL	Specim PS Kappa DX4	400–700	31	1392×1300	/
Remote Sensing HSIs	Xiong'an	Unknown	400–1000	256	3750×1580	0.5
	WDC	Hydice	400–2400	191	1208×307	5
	PaviaC	ROSIS	430–860	102	1096×715	1.3
	PaviaU	ROSIS	430–860	103	610×340	1.3
	Houston	ITRES CASI-1500	364–1046	144	349×1905	2.5
	Chikusei	HH-VNIR-C	343–1018	128	2517×2335	2.5
	Eagle	AsiaEAGLE II	401–999	128	2082×1606	1
	Berlin	Unknown	455–2447	111	6805×1830	3.6
	Urban	Hydice	400-2500	210	307×307	2
	APEX	Unknown	350-2500	285	1000×1500	2
	EO-1	Hyperion	357-2567	242	3471×991	30

Table 5. Properties of 13 Natural Scene and Remote Sensing Hyperspectral Datasets.

H. Detailed Experimental Setup

In this section, we provide a detailed description of the experimental settings for the 9 HSI restoration tasks.

Gaussian Denoising. Each image was corrupted by zero-mean independent and identically distributed (i.i.d.) Gaussian noise with sigma ranging from 30 to 70. For testing, sigma = 30, 50, and 70 were selected for evaluation.

Complex Denoising. Each image was corrupted with one of the following four noise scenarios:

1) Case 1 (*Non-i.i.d. Gaussian Noise*): All bands were corrupted by non-i.i.d. Gaussian noise with standard deviations randomly selected from 10 to 70.

2) Case 2 (*Gaussian Noise + Stripe Noise*): All bands were corrupted by non-i.i.d. Gaussian noise, and one-third of the bands were randomly selected to add column stripe noise with intensities ranging from 5% to 15%.

3) Case 3 (*Gaussian Noise + Deadline Noise*): The noise generation process was similar to Case 2, but stripe noise was replaced by deadline noise.

4) Case 4 (*Gaussian Noise + Impulse Noise*): All bands were corrupted by non-i.i.d. Gaussian noise, and one-third of the bands were randomly selected to add impulse noise with intensities ranging from 10% to 70%.

Gaussian Deblurring. An empirical formula was used to calculate the standard deviation σ based on the Gaussian kernel size K_S, formulated as:

$$\sigma = 0.3 \times \left(\frac{K_S - 1}{2} - 1 \right) + 0.8. \qquad (10)$$

For natural hyperspectral datasets, K_S was set to 9, 15, and 21, while for remote sensing hyperspectral datasets, K_S was set to 7, 11, and 15.

Super-Resolution. Bicubic interpolation was used to downsample the images, with downscaling factors of 2, 4, and 8. To ensure that the input and output image sizes of the all-in-one model remained consistent, an unpooling operation was applied to resize the downsampled HSIs to their original dimensions.

Inpainting. Random masks with rates of 0.7, 0.8, and 0.9 were applied to each image for the inpainting task.

Dehazing. To realistically simulate haze contamination, the haze synthesis method from [17] was adopted. Specifically, 100 haze masks were extracted from the cirrus band of Landsat-8 OLI and superimposed onto the original image according to the wavelength ratio to generate haze-affected HSIs, modeled as:

$$I_i = J_i e^{\left(\frac{\lambda_1}{\lambda_i}\right)^\gamma \ln t_1} + A \left(1 - e^{\left(\frac{\lambda_1}{\lambda_i}\right)^\gamma \ln t_1} \right), \qquad (11)$$

where I is the hazy HSI, J is the clear HSI, A is the global atmospheric light, λ is the wavelength, and γ is the spatial function, which is set to 1. The reference transmission map t_1 is calculated from the cirrus band reflectance:

$$t_1 = 1 - \omega B_9, \qquad (12)$$

where ω is a weighting factor controlling the haze intensity, and B_9 is the cirrus band reflectance. In the experiments, ω was set to [0.5, 0.75, 1], corresponding to different levels of haze contamination.

Band Completion. A certain proportion of bands were discarded for each image, with discard rates of 0.1, 0.2, and 0.3. The experimental results were evaluated only on the missing bands.

Type	Methods	Gaussian Denoising (ICVL [3])			Gaussian Denoising (ARAD [4])			Gaussian Denoising (Xiong'an [72])		
		Sigma = 30	Sigma = 50	Sigma = 70	Sigma = 30	Sigma = 50	Sigma = 70	Sigma = 30	Sigma = 50	Sigma = 70
		PSNR / SSIM ↑	PSNR / SSIM ↑	PSNR / SSIM ↑	PSNR / SSIM ↑	PSNR / SSIM ↑	PSNR / SSIM ↑	PSNR / SSIM ↑	PSNR / SSIM ↑	PSNR / SSIM ↑
Task Specific	QRNN3D [63]	42.18 / 0.967	39.70 / 0.942	38.09 / 0.933	41.67 / 0.967	39.15 / 0.935	36.71 / 0.894	37.86 / 0.870	36.03 / 0.825	34.29 / 0.792
	SST [33]	43.32 / 0.976	41.09 / 0.952	39.51 / 0.949	43.02 / 0.972	40.58 / 0.951	38.99 / 0.941	39.26 / 0.878	37.34 / 0.848	35.99 / 0.824
	SERT [34]	43.53 / 0.978	41.32 / 0.966	39.82 / 0.956	43.21 / 0.975	40.84 / 0.959	39.21 / 0.945	39.54 / 0.885	37.58 / 0.859	36.37 / 0.833
	LDERT [35]	44.12 / 0.982	41.68 / 0.968	39.95 / 0.957	43.74 / 0.979	41.35 / 0.966	39.32 / 0.950	39.92 / 0.889	37.96 / 0.868	36.54 / 0.838
All in One	AirNet [32]	42.02 / 0.966	39.68 / 0.942	37.59 / 0.923	41.39 / 0.963	39.08 / 0.933	37.09 / 0.903	34.04 / 0.700	31.61 / 0.665	30.17 / 0.639
	PromptIR [52]	42.40 / 0.971	40.14 / 0.954	38.20 / 0.934	41.84 / 0.967	39.55 / 0.947	37.67 / 0.921	34.90 / 0.715	32.76 / 0.680	31.31 / 0.657
	PIP [36]	43.00 / 0.974	40.69 / 0.958	38.94 / 0.941	42.33 / 0.970	40.07 / 0.953	38.36 / 0.933	34.51 / 0.704	32.43 / 0.671	30.98 / 0.647
	HAIR [7]	42.53 / 0.972	40.23 / 0.957	38.78 / 0.939	42.03 / 0.968	39.76 / 0.950	37.95 / 0.928	34.51 / 0.712	32.22 / 0.675	30.89 / 0.650
	InstructIR [12]	42.99 / 0.974	40.84 / 0.960	39.23 / 0.946	42.21 / 0.970	40.16 / 0.955	38.60 / 0.938	33.79 / 0.703	31.47 / 0.662	29.96 / 0.633
	PromptHSI [30]	42.61 / 0.976	40.27 / 0.960	39.08 / 0.945	41.90 / 0.971	39.84 / 0.959	38.37 / 0.938	39.54 / 0.902	37.80 / 0.877	36.87 / 0.864
	MP-HSIR (Ours)	43.62 / 0.977	41.41 / 0.963	39.82 / 0.951	43.12 / 0.975	40.88 / 0.960	39.28 / 0.946	40.55 / 0.922	38.70 / 0.896	37.17 / 0.874

Table 6. **[All-in-one]** Quantitative comparison of all-in-one and state-of-the-art task-specific methods under different Gaussian noise levels on *Gaussian denoising* tasks. The best and second-best performances are highlighted in red and blue, respectively.

Type	Methods	Complex Denoising (ICVL [3])				Complex Denoising (ARAD [4])				Complex Denoising (WDC [81])			
		Case = 1	Case = 2	Case = 3	Case = 4	Case = 1	Case = 2	Case = 3	Case = 4	Case = 1	Case = 2	Case = 3	Case = 4
		PSNR / SSIM ↑	PSNR / SSIM ↑	PSNR / SSIM ↑	PSNR / SSIM ↑	PSNR / SSIM ↑	PSNR / SSIM ↑	PSNR / SSIM ↑	PSNR / SSIM ↑	PSNR / SSIM ↑	PSNR / SSIM ↑	PSNR / SSIM ↑	PSNR / SSIM ↑
Task Specific	QRNN3D [63]	42.24 / 0.969	41.98 / 0.968	41.62 / 0.968	40.55 / 0.960	41.74 / 0.966	41.55 / 0.965	41.38 / 0.964	39.76 / 0.946	31.98 / 0.885	31.77 / 0.882	31.48 / 0.878	28.05 / 0.822
	SST [33]	43.38 / 0.976	42.69 / 0.973	42.51 / 0.972	41.16 / 0.964	42.84 / 0.973	42.38 / 0.971	42.01 / 0.970	40.56 / 0.956	33.85 / 0.907	33.69 / 0.905	33.37 / 0.901	29.92 / 0.841
	SERT [34]	43.96 / 0.980	43.48 / 0.978	43.45 / 0.977	42.37 / 0.969	43.56 / 0.978	43.19 / 0.976	42.88 / 0.974	41.85 / 0.963	34.48 / 0.922	34.26 / 0.920	33.98 / 0.915	30.53 / 0.854
	LDERT [35]	44.04 / 0.981	43.57 / 0.979	43.55 / 0.979	42.51 / 0.971	43.67 / 0.979	43.33 / 0.977	43.06 / 0.974	42.02 / 0.965	34.65 / 0.923	34.42 / 0.920	34.13 / 0.917	30.74 / 0.856
All in One	AirNet [32]	42.11 / 0.968	41.24 / 0.964	40.89 / 0.961	38.49 / 0.942	41.62 / 0.965	40.83 / 0.959	40.31 / 0.957	37.59 / 0.905	29.02 / 0.752	28.93 / 0.744	28.67 / 0.740	25.67 / 0.667
	PromptIR [52]	42.76 / 0.973	41.93 / 0.969	41.43 / 0.969	39.04 / 0.947	42.26 / 0.969	41.54 / 0.964	40.90 / 0.964	38.12 / 0.919	29.84 / 0.761	29.71 / 0.754	29.39 / 0.747	26.38 / 0.676
	PIP [36]	42.96 / 0.974	42.13 / 0.970	41.38 / 0.969	40.19 / 0.959	42.39 / 0.971	41.71 / 0.966	41.11 / 0.966	39.45 / 0.943	29.57 / 0.751	29.31 / 0.745	29.17 / 0.740	25.95 / 0.658
	HAIR [7]	41.78 / 0.965	41.47 / 0.965	40.68 / 0.958	38.58 / 0.943	41.19 / 0.959	40.95 / 0.961	40.53 / 0.959	37.92 / 0.909	29.38 / 0.756	29.22 / 0.750	28.73 / 0.744	25.40 / 0.664
	InstructIR [12]	41.29 / 0.963	40.89 / 0.961	39.94 / 0.958	38.46 / 0.945	40.72 / 0.960	40.38 / 0.957	39.94 / 0.956	38.21 / 0.934	28.66 / 0.736	28.47 / 0.730	28.19 / 0.725	24.63 / 0.637
	PromptHSI [30]	40.61 / 0.967	40.36 / 0.965	39.30 / 0.960	36.27 / 0.927	40.22 / 0.951	39.98 / 0.955	39.42 / 0.953	35.39 / 0.884	34.93 / 0.931	34.87 / 0.930	34.49 / 0.928	30.78 / 0.857
	MP-HSIR (Ours)	43.07 / 0.975	42.46 / 0.972	42.20 / 0.972	41.42 / 0.966	42.74 / 0.973	42.32 / 0.971	41.93 / 0.970	40.98 / 0.960	35.21 / 0.933	34.99 / 0.931	34.72 / 0.928	31.36 / 0.880

Table 7. **[All-in-one]** Quantitative comparison of all-in-one and state-of-the-art task-specific methods under different cases on *Complex denoising* tasks. The best and second-best performances are highlighted in red and blue, respectively.
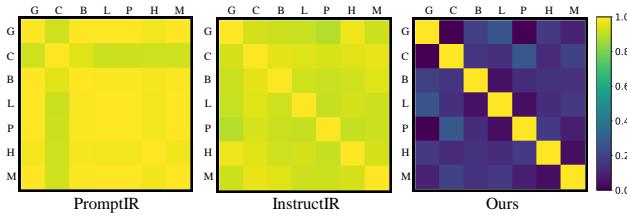

Figure 8. Similarity matrices of prompt vector for seven HSI restoration tasks, with task names as in manuscript.

Motion Deblurring. The pre-trained model was fine-tuned and tested on this task with a blur kernel radius of 15 and a blur angle of 45 degrees.

Poisson Denoising. The pre-trained model was directly tested on this task with a Poisson noise intensity scaling factor of 10.

I. Visualization Results of Prompts

In Table 8, we present the similarity matrices of prompt vectors for different degradation types, comparing PromptIR [52], InstructIR [12], and the proposed method. PromptIR relies exclusively on visual prompts, InstructIR utilizes textual prompts for guidance, and the proposed method integrates text-visual synergistic prompts to enhance degradation modeling. As illustrated in the figure, both PromptIR and InstructIR struggle to effectively differentiate between various HSI degradation types, whereas our method demonstrates distinct separation for each individual task, highlighting its superior capability in handling diverse degradation scenarios.

J. More Experimental Results

In this section, we present additional experimental results, including the results of more quantitative results, model efficiency, more results of ablation study, controllability analysis, and more visual comparisons.

J.1. More Quantitative Results

In this section, we provide a detailed quantitative comparison for 7 all-in-one HSI restoration tasks. The experimental results across different degradation levels are systematically presented for each task, including Gaussian denoising in Table 6, complex denoising in Table 7, Gaussian deblurring in Table 8, super-resolution in Table 9, inpainting in Table 11, dehazing in Table 12, and band completion in Table 13.

In addition, we further evaluate the performance on real-world hyperspectral data using the no-reference metric QSFL [71]. The results on the Urban and EO-1 datasets are reported

Type	Methods	Gaussian Deblurring (ICVL [3])			Gaussian Deblurring (PaviaC [24])			Gaussian Deblurring (Eagle [51])		
		Radius = 9	Radius = 15	Radius = 21	Radius = 7	Radius = 11	Radius = 15	Radius = 7	Radius = 11	Radius = 15
		PSNR / SSIM ↑	PSNR / SSIM ↑	PSNR / SSIM ↑	PSNR / SSIM ↑	PSNR / SSIM ↑	PSNR / SSIM ↑	PSNR / SSIM ↑	PSNR / SSIM ↑	PSNR / SSIM ↑
Task Specific	Stripformer [58]	49.21 / 0.994	45.85 / 0.989	43.04 / 0.980	38.73 / 0.934	36.95 / 0.914	35.72 / 0.891	44.68 / 0.974	41.37 / 0.958	39.83 / 0.942
	FFTformer [27]	49.83 / 0.994	46.43 / 0.989	43.69 / 0.981	39.82 / 0.942	37.63 / 0.919	36.44 / 0.901	45.51 / 0.980	42.18 / 0.962	40.59 / 0.944
	LoFormer [47]	50.35 / 0.995	46.94 / 0.991	44.15 / 0.983	39.54 / 0.941	37.41 / 0.918	36.21 / 0.892	45.32 / 0.979	42.03 / 0.961	40.42 / 0.946
	MLWNet [14]	50.68 / 0.996	47.54 / 0.991	44.76 / 0.983	40.85 / 0.949	38.92 / 0.929	37.28 / 0.901	46.61 / 0.983	43.68 / 0.969	41.83 / 0.955
All in One	AirNet [32]	50.64 / 0.995	47.10 / 0.991	43.89 / 0.982	39.45 / 0.940	37.76 / 0.921	36.08 / 0.893	44.83 / 0.977	42.32 / 0.966	40.11 / 0.946
	PromptIR [52]	51.00 / 0.996	47.70 / 0.992	44.32 / 0.983	40.41 / 0.948	38.62 / 0.929	37.13 / 0.904	46.17 / 0.981	43.45 / 0.968	41.60 / 0.955
	PIP [36]	51.05 / 0.996	47.29 / 0.991	44.21 / 0.983	40.31 / 0.944	38.51 / 0.926	36.73 / 0.902	45.90 / 0.982	42.75 / 0.968	40.86 / 0.951
	HAIR [7]	49.43 / 0.994	46.06 / 0.989	43.87 / 0.981	39.97 / 0.943	38.18 / 0.923	35.64 / 0.891	45.14 / 0.979	42.69 / 0.966	40.48 / 0.947
	InstructIR [12]	24.19 / 0.533	33.44 / 0.878	44.51 / 0.983	19.66 / 0.329	25.12 / 0.583	36.32 / 0.894	23.35 / 0.477	34.05 / 0.872	40.64 / 0.949
	PromptHSI [30]	25.16 / 0.619	30.89 / 0.852	41.52 / 0.980	38.73 / 0.936	36.63 / 0.913	34.84 / 0.888	42.45 / 0.972	39.34 / 0.952	37.46 / 0.938
	MP-HSIR (Ours)	51.53 / 0.996	47.60 / 0.992	45.07 / 0.982	40.85 / 0.949	38.95 / 0.928	37.19 / 0.905	46.26 / 0.982	43.54 / 0.969	41.36 / 0.952

Table 8. **[All-in-one]** Quantitative comparison of all-in-one and state-of-the-art task-specific methods under different blur kernel radius on *Gaussian deblurring* tasks. The best and second-best performances are highlighted in red and blue, respectively.

Type	Methods	Super-Resolution (ARAD [4])			Super-Resolution (PaviaU [24])			Super-Resolution (Houston [66])		
		Scale = 2	Scale = 4	Scale = 8	Scale = 2	Scale = 4	Scale = 8	Scale = 2	Scale = 4	Scale = 8
		PSNR / SSIM ↑	PSNR / SSIM ↑	PSNR / SSIM ↑	PSNR / SSIM ↑	PSNR / SSIM ↑	PSNR / SSIM ↑	PSNR / SSIM ↑	PSNR / SSIM ↑	PSNR / SSIM ↑
Task Specific	SNLSR [23]	43.93 / 0.980	34.56 / 0.902	29.67 / 0.813	34.58 / 0.869	29.85 / 0.719	27.23 / 0.601	34.91 / 0.908	31.33 / 0.782	28.86 / 0.671
	MAN [60]	44.81 / 0.985	35.35 / 0.912	30.49 / 0.830	34.92 / 0.872	30.26 / 0.723	27.59 / 0.604	35.26 / 0.911	31.68 / 0.785	29.15 / 0.677
	ESSAformer [78]	45.32 / 0.988	36.02 / 0.927	30.85 / 0.838	35.47 / 0.879	30.60 / 0.728	27.96 / 0.606	35.60 / 0.913	31.94 / 0.787	29.57 / 0.679
	SRFormer [80]	45.84 / 0.989	36.73 / 0.931	31.48 / 0.845	35.92 / 0.887	31.08 / 0.745	28.41 / 0.620	36.15 / 0.920	32.44 / 0.805	29.81 / 0.684
All in One	AirNet [32]	44.82 / 0.985	35.26 / 0.919	30.12 / 0.828	34.85 / 0.871	30.19 / 0.724	27.76 / 0.609	35.22 / 0.911	31.65 / 0.786	29.13 / 0.676
	PromptIR [52]	45.33 / 0.988	36.00 / 0.927	30.77 / 0.838	35.57 / 0.883	30.81 / 0.735	28.20 / 0.619	35.96 / 0.915	32.38 / 0.798	29.85 / 0.684
	PIP [36]	46.01 / 0.989	37.34 / 0.939	31.73 / 0.853	35.71 / 0.885	31.02 / 0.744	28.20 / 0.618	36.10 / 0.917	32.55 / 0.806	30.02 / 0.692
	HAIR [7]	43.77 / 0.984	35.89 / 0.924	30.87 / 0.836	35.49 / 0.882	30.79 / 0.736	28.13 / 0.616	35.81 / 0.913	32.17 / 0.795	29.64 / 0.680
	InstructIR [12]	43.47 / 0.984	35.46 / 0.921	30.61 / 0.834	35.25 / 0.879	30.71 / 0.732	28.05 / 0.613	35.68 / 0.909	32.15 / 0.789	29.73 / 0.681
	PromptHSI [30]	40.25 / 0.975	35.41 / 0.931	29.35 / 0.806	34.84 / 0.871	30.13 / 0.722	27.27 / 0.602	35.34 / 0.912	31.62 / 0.778	28.59 / 0.635
	MP-HSIR (Ours)	46.72 / 0.991	36.88 / 0.939	31.14 / 0.843	36.27 / 0.894	31.26 / 0.757	28.38 / 0.630	36.57 / 0.926	32.68 / 0.813	29.92 / 0.690

Table 9. **[All-in-one]** Quantitative comparison of all-in-one and state-of-the-art task-specific methods under different downsampling scales on *Super-Resolution* tasks. The best and second-best performances are highlighted in red and blue, respectively.

Dataset	PromptIR	InstructIR	PromptHSI	**MP-HSIR**
Urban	14.95	15.56	12.34	**11.42**
EO-1	17.99	19.71	18.13	**16.54**

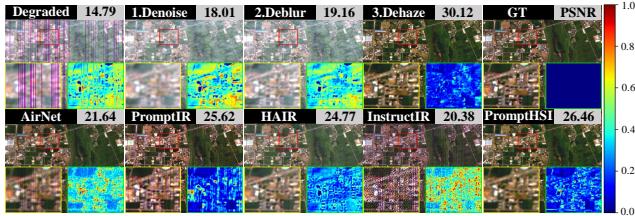Table 10. No-reference quality assessment on real datasets.

Figure 9. Progressive results (ours) and final results (others).

in Table 10, providing a more comprehensive assessment of generalization ability under practical conditions.

J.2. Model Efficiency

In this section, we present the parameter counts and computational costs of the all-in-one models for both natural scene and remote sensing hyperspectral datasets. Notably, the net-

work width for remote sensing datasets is 1.5 times greater than that for natural scene datasets across all models. As demonstrated in Table 14, our method achieves a lower parameter count while maintaining competitive computational efficiency.

Furthermore, to evaluate the practical inference performance, Table 15 reports the average inference time of each method on remote sensing datasets. Our method maintains a favorable trade-off between efficiency and accuracy, demonstrating its suitability for large-scale deployment.

J.3. More results of Ablation Study

In this section, we present ablation studies on the textual prompts P_T, learnable visual prompts P_V, global spectral self-attention, local spectral self-attention, and spectral prompts P_S across multiple tasks, as shown in Tables 16, 17, and 18. Overall, the addition of each module progressively improves the two accuracy metrics across all tasks.

J.4. Controllable Results

In this section, we demonstrate the controllable restoration capability of the proposed method. Specifically, we conduct controlled restoration tasks under two composite degradation

Type	Methods	Inpainting (ICVL [3])			Inpainting (Chikusei [73])		
		Rate = 0.7	Rate = 0.8	Rate = 0.9	Rate = 0.7	Rate = 0.8	Rate = 0.9
		PSNR / SSIM ↑	PSNR / SSIM ↑	PSNR / SSIM ↑	PSNR / SSIM ↑	PSNR / SSIM ↑	PSNR / SSIM ↑
Task Specific	NAFNet [8]	45.03 / 0.989	44.65 / 0.988	43.50 / 0.985	40.34 / 0.952	40.15 / 0.955	38.97 / 0.952
	Restormer [76]	46.51 / 0.991	46.00 / 0.991	44.85 / 0.988	36.52 / 0.902	36.34 / 0.892	36.13 / 0.903
	DDS2M [48]	45.41 / 0.989	43.34 / 0.983	37.80 / 0.935	36.77 / 0.906	35.23 / 0.901	32.83 / 0.854
	HIR-Diff [50]	41.82 / 0.973	38.87 / 0.949	36.04 / 0.924	38.59 / 0.923	37.96 / 0.920	36.41 / 0.904
All in One	AirNet [32]	43.10 / 0.983	43.06 / 0.983	41.65 / 0.977	38.12 / 0.919	37.86 / 0.921	36.39 / 0.918
	PromptIR [52]	46.96 / 0.992	46.93 / 0.992	45.24 / 0.988	38.86 / 0.925	38.30 / 0.931	37.05 / 0.934
	PIP [36]	44.37 / 0.985	43.47 / 0.983	42.26 / 0.978	38.74 / 0.922	38.58 / 0.930	37.98 / 0.938
	HAIR [7]	44.83 / 0.983	44.30 / 0.983	42.92 / 0.981	38.43 / 0.921	38.28 / 0.928	37.43 / 0.932
	InstructIR [12]	44.85 / 0.989	44.29 / 0.987	43.08 / 0.983	36.30 / 0.904	36.18 / 0.908	35.84 / 0.909
	PromptHSI [30]	42.83 / 0.983	41.72 / 0.976	39.89 / 0.956	38.99 / 0.966	37.64 / 0.952	35.35 / 0.920
	MP-HSIR (Ours)	53.06 / 0.997	51.94 / 0.996	49.60 / 0.994	44.75 / 0.981	44.06 / 0.981	42.08 / 0.975

Table 11. **[All-in-one]** Quantitative comparison of all-in-one and state-of-the-art task-specific methods under different mask rates on *Inpainting* tasks. The best and second-best performances are highlighted in red and blue, respectively.

Type	Methods	Dehazing (PaviaU [24])			Dehazing (Eagle [51])		
		Omega = 0.5	Omega = 0.75	Omega = 1.0	Omega = 0.5	Omega = 0.75	Omega = 1.0
		PSNR / SSIM ↑	PSNR / SSIM ↑	PSNR / SSIM ↑	PSNR / SSIM ↑	PSNR / SSIM ↑	PSNR / SSIM ↑
Task Specific	SGNet [45]	36.52 / 0.974	34.10 / 0.964	32.22 / 0.949	39.43 / 0.989	37.33 / 0.976	34.90 / 0.962
	SCANet [18]	39.01 / 0.986	36.54 / 0.978	34.21 / 0.969	41.92 / 0.991	39.68 / 0.987	37.31 / 0.978
	MB-Taylor [54]	40.51 / 0.991	38.03 / 0.984	35.44 / 0.975	43.76 / 0.995	40.97 / 0.992	38.36 / 0.986
	DCMPNet [79]	39.63 / 0.993	37.14 / 0.985	34.82 / 0.976	42.93 / 0.995	40.15 / 0.991	37.64 / 0.985
All in One	AirNet [32]	38.61 / 0.982	35.65 / 0.967	32.51 / 0.947	41.88 / 0.991	38.68 / 0.982	35.92 / 0.969
	PromptIR [52]	40.34 / 0.991	37.43 / 0.983	34.47 / 0.971	43.55 / 0.995	40.69 / 0.992	37.94 / 0.988
	PIP [36]	40.30 / 0.991	37.64 / 0.983	34.93 / 0.971	43.21 / 0.994	40.95 / 0.991	38.07 / 0.985
	HAIR [7]	39.47 / 0.989	36.79 / 0.980	34.02 / 0.965	43.38 / 0.995	40.54 / 0.992	38.67 / 0.988
	InstructIR [12]	38.24 / 0.986	34.57 / 0.974	31.36 / 0.954	40.90 / 0.991	38.07 / 0.985	33.99 / 0.971
	PromptHSI [30]	38.62 / 0.982	36.48 / 0.975	35.22 / 0.964	40.88 / 0.986	40.49 / 0.984	37.98 / 0.981
	MP-HSIR (Ours)	42.64 / 0.993	39.46 / 0.988	36.68 / 0.978	45.66 / 0.997	42.24 / 0.995	39.34 / 0.992

Table 12. **[All-in-one]** Quantitative comparison of all-in-one and state-of-the-art task-specific methods under different haze levels on *Dehazing* tasks. The best and second-best performances are highlighted in red and blue, respectively.

Type	Methods	Band Completion (ARAD [4])			Band Completion (Berlin [49])		
		Rate = 0.1	Rate = 0.2	Rate = 0.3	Rate = 0.1	Rate = 0.2	Rate = 0.3
		PSNR / SSIM ↑	PSNR / SSIM ↑	PSNR / SSIM ↑	PSNR / SSIM ↑	PSNR / SSIM ↑	PSNR / SSIM ↑
Task Specific	NAFNet [8]	47.82 / 0.996	47.02 / 0.995	46.29 / 0.994	39.71 / 0.972	37.51 / 0.874	37.84 / 0.875
	Restormer [76]	49.24 / 0.997	48.29 / 0.995	47.49 / 0.993	34.98 / 0.605	35.24 / 0.606	35.00 / 0.607
	SwinIR [37]	50.95 / 0.997	49.80 / 0.995	48.49 / 0.993	36.88 / 0.950	34.69 / 0.855	34.78 / 0.854
	MambaIR [16]	51.46 / 0.998	50.32 / 0.995	49.01 / 0.993	37.54 / 0.953	35.38 / 0.857	35.43 / 0.855
All in One	AirNet [32]	46.14 / 0.994	45.21 / 0.992	44.46 / 0.990	37.62 / 0.691	35.26 / 0.586	34.86 / 0.595
	PromptIR [52]	47.68 / 0.996	46.71 / 0.994	45.41 / 0.992	42.81 / 0.707	39.55 / 0.910	39.00 / 0.640
	PIP [36]	48.35 / 0.995	47.37 / 0.994	46.37 / 0.991	38.60 / 0.706	36.58 / 0.657	36.43 / 0.641
	HAIR [7]	46.27 / 0.994	44.92 / 0.992	44.04 / 0.990	40.04 / 0.705	36.54 / 0.607	37.45 / 0.639
	InstructIR [12]	52.66 / 0.998	51.37 / 0.997	49.90 / 0.996	36.17 / 0.606	35.33 / 0.559	36.40 / 0.576
	PromptHSI [30]	49.05 / 0.996	47.09 / 0.993	45.89 / 0.992	47.11 / 0.997	43.14 / 0.973	39.82 / 0.956
	MP-HSIR (Ours)	57.83 / 0.999	56.61 / 0.999	54.99 / 0.998	52.14 / 0.999	49.20 / 0.997	47.26 / 0.965

Table 13. **[All-in-one]** Quantitative comparison of all-in-one and state-of-the-art task-specific methods under different mask rates on *Band Completion* tasks. The best and second-best performances are highlighted in red and blue, respectively.

Methods	Natural Scene		Remote Sensing	
	Params (M)	FLOPS (G)	Params (M)	FLOPS (G)
AirNet [32]	5.82	19.04	12.23	43.79
PromptIR [52]	33.00	10.03	72.60	22.21
PIP [36]	27.80	10.66	58.26	22.08
HAIR [7]	7.68	2.72	17.28	6.46
InstructIR [12]	68.82	2.81	154.03	6.57
PromptHSI [30]	25.90	10.10	50.89	21.91
MP-HSIR (Ours)	13.88	14.40	30.91	32.74

Table 14. Model complexity comparisons

Metric	PromptIR	InstructIR	PromptHSI	**MP-HSIR**
Inference Time (s)	0.087	**0.065**	0.282	0.083

Table 15. Inference time for remote sensing scenes (64×64×100).

Method	PSNR ↑	SSIM ↑	Params (M)
Baseline (Only Spatial SA)	33.78	0.782	20.93
+ Textual Prompt P_T	34.53	0.807	21.51
+ Visual Prompt P_V	34.47	0.805	23.68
+ Textual Prompt P_T + Visual Prompt P_V	34.92	0.822	24.26
+ Global Spectral SA + P_T + P_T	35.20	0.835	30.07
+ Local Spectral SA + P_T + P_V	35.82	0.846	24.43
+ Local Spectral SA + P_T + P_V + Spectral Prompt P_S	36.67	0.863	25.10
Full Model	**37.17**	**0.874**	30.91

Table 16. Ablation study to verify the effectiveness of modules on Xiong'an dataset in *Gaussian denoising* task with sigma = 70.

Method	PSNR ↑	SSIM ↑	Params (M)
Baseline (Only Spatial SA)	30.10	0.788	20.93
+ Textual Prompt P_T	37.64	0.928	21.51
+ Visual Prompt P_V	37.42	0.925	23.68
+ Textual Prompt P_T + Visual Prompt P_V	38.91	0.942	24.26
+ Global Spectral SA + P_T + P_T	39.20	0.944	30.07
+ Local Spectral SA + P_T + P_V	39.79	0.948	24.43
+ Local Spectral SA + P_T + P_V + Spectral Prompt P_S	40.51	0.950	25.10
Full Model	**41.36**	**0.952**	30.91

Table 17. Ablation study to verify the effectiveness of modules on Eagle dataset in *Gaussian deblurring* task with radius = 15.

Method	PSNR ↑	SSIM ↑	Params (M)
Baseline (Only Spatial SA)	32.52	0.967	20.93
+ Textual Prompt P_T	34.24	0.965	21.51
+ Visual Prompt P_V	34.13	0.964	23.68
+ Textual Prompt P_T + Visual Prompt P_V	34.92	0.969	24.26
+ Global Spectral SA + P_T + P_T	35.53	0.973	30.07
+ Local Spectral SA + P_T + P_V	35.64	0.974	24.43
+ Local Spectral SA + P_T + P_V + Spectral Prompt P_S	36.13	0.976	25.10
Full Model	**36.68**	**0.978**	30.91

Table 18. Ablation study to verify the effectiveness of modules on PaviaU dataset in *Dehazing* task with Omega = 1.0.

scenarios: Gaussian noise with Gaussian blur and complex noise with Gaussian blur, aiming to remove noise while preserving blur. As illustrated in Figures 10 and 11, our method
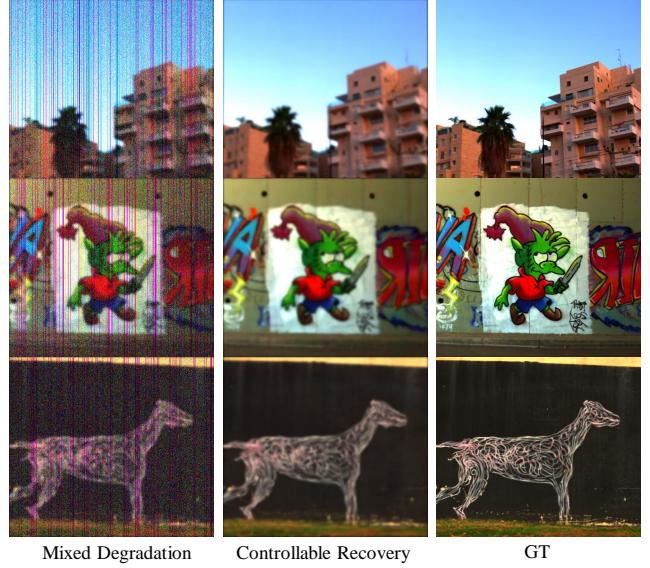

Mixed Degradation   Controllable Recovery   GT

Figure 10. Controllable Reconstruction: Removing *Gaussian* from *Gaussian Noise + Gaussian Blur* Degradation.
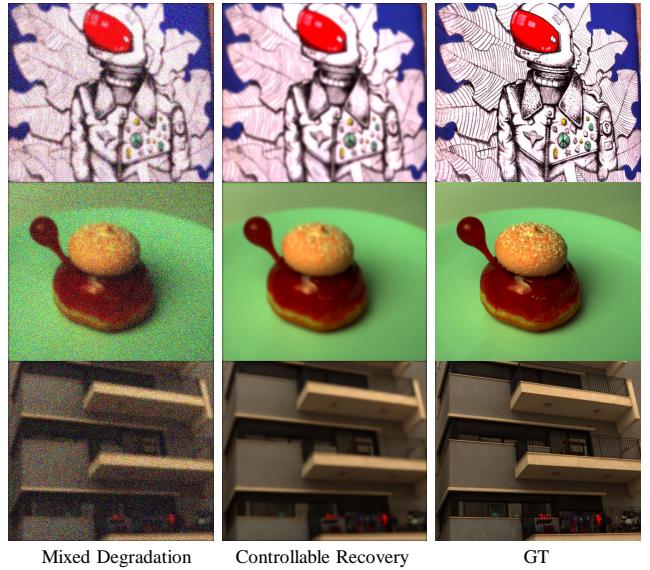

Mixed Degradation   Controllable Recovery   GT

Figure 11. Controllable Reconstruction: Removing *Complex Noise* from *Complex Noise + Gaussian Blur* Degradation.

can precisely remove specific degradation types through accurate guidance from textual prompts, highlighting its controllability and interpretability.

Building on this controllable restoration paradigm, we further explore sequential degradation removal, where multiple degradations are addressed step by step under prompt guidance. As shown in Figure 9, our method achieves superior results in this more challenging setting, outperforming other approaches in both visual quality and flexibility.
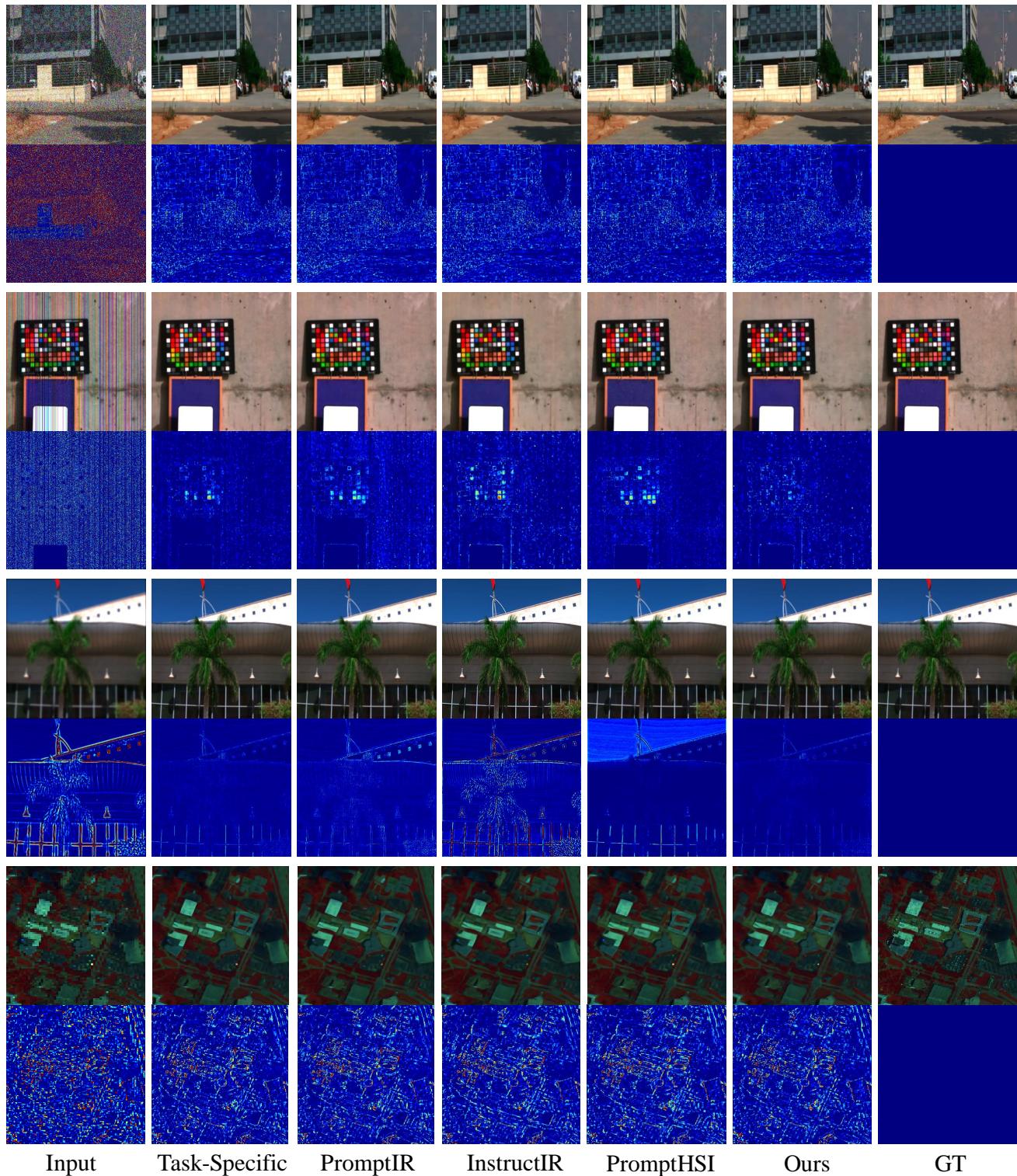
Figure 12. Visual comparison results of ***Gaussian denoising***, ***complex denoising***, ***Gaussian deblurring***, and ***super-resolution***, including the corresponding residual maps. Task-Specific represents the optimal task-specific method.
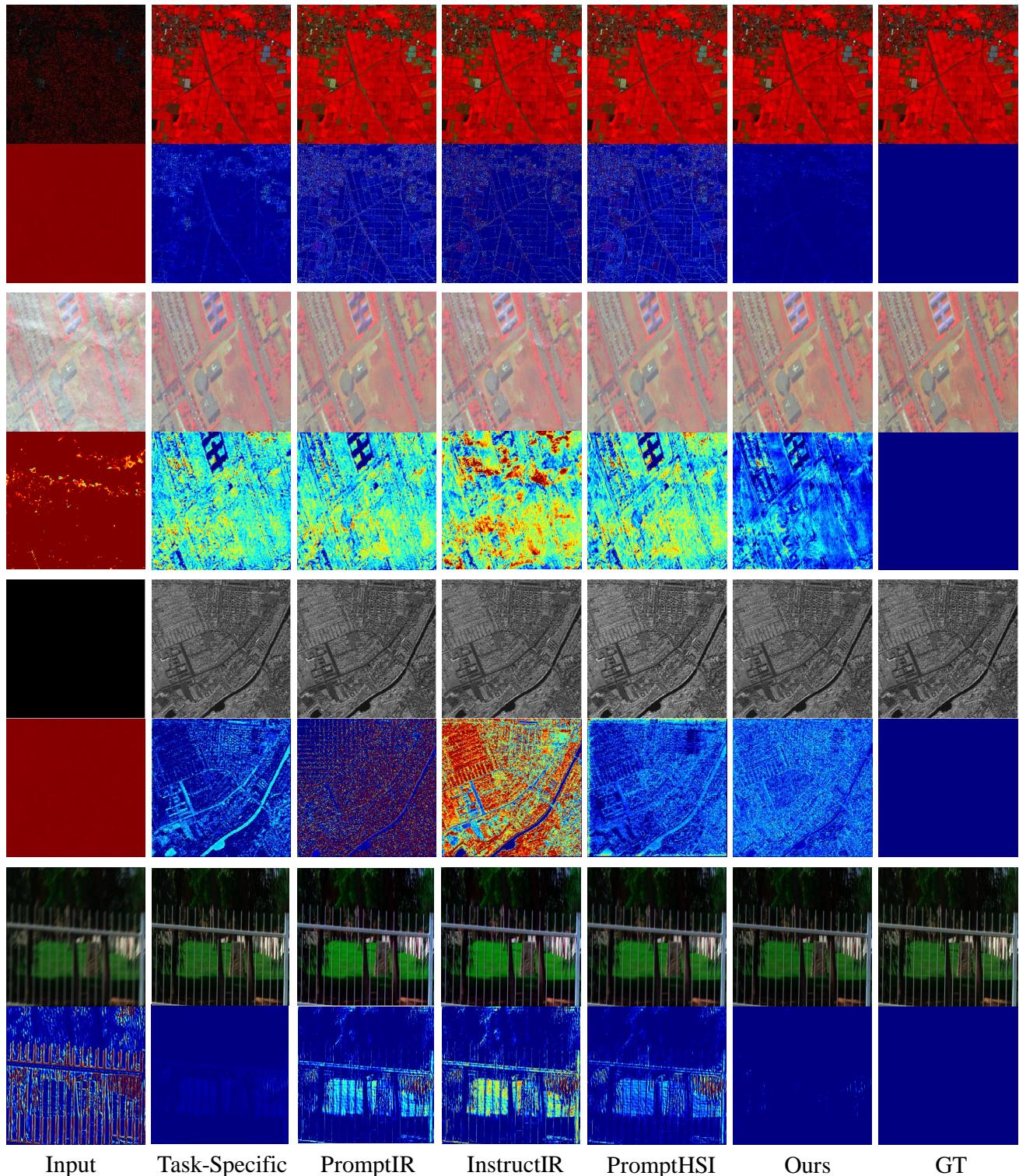
Figure 13. Visual comparison results of *Inpainting*, *Dehazing*, *Band Completion*, and *Motion Deblurring*, including the corresponding residual maps. Task-Specific represents the optimal task-specific method.
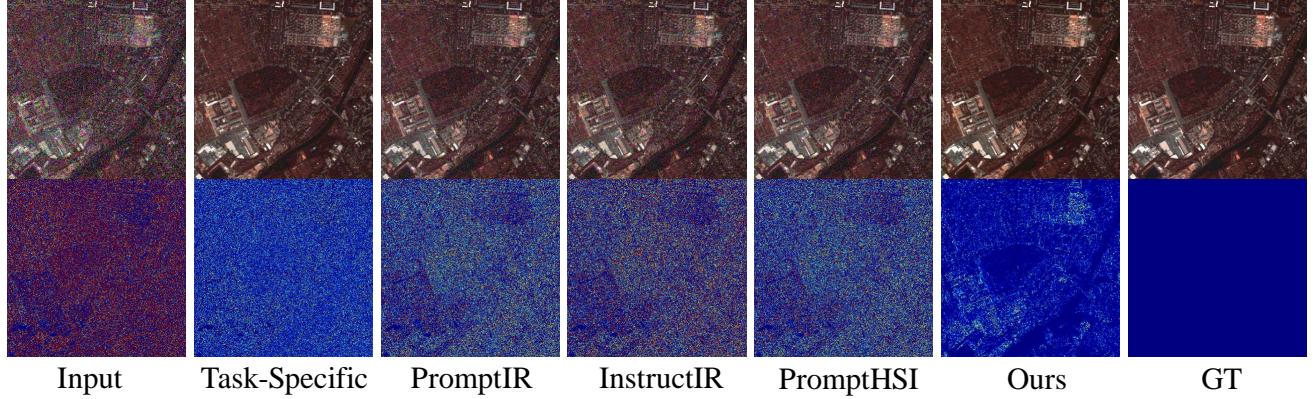
Figure 14. Visual comparison results of **_Poisson Denoising_**, including the corresponding residual maps. Task-Specific represents the optimal task-specific method.
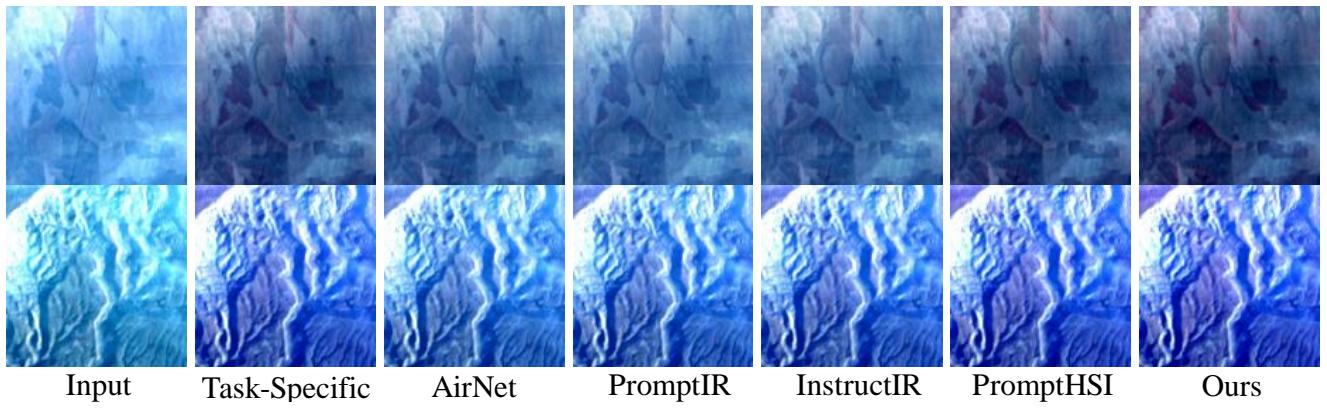

Figure 15. Visual comparison results of **_Real Dehazing_**. Task-Specific represents the optimal task-specific method.

J.5. More Visual Results

In this section, we present further visual results for each task, including all-in-one experiments, generalization testing, and real-world scenarios. As shown in Figures 12, 13, 14, and 15, the visualization results indicate that our method achieves the best performance in restoring texture details and structural features.